ABSTRACT

SHAH, CHINMAY SANJAY. EMG-driven Musculoskeletal Model for Volitional Control of a Robotic Ankle Prosthesis. (Under the direction of Dr. He Huang and Dr. Katherine Saul).

Lower-limb amputations severely affects the ability of individuals to perform functional tasks, which affects their quality of life. Robotic lower limb prostheses have been developed that are capable of generating the same torque and power requirements as those of able-bodied joints. These existing robotic lower-limb prostheses use autonomous control to address cyclic, locomotive tasks, but they are inadequate to operate the prosthesis for daily activities that are non-cyclic and unpredictable. To address this challenge, this study aims to design a novel electromyography (EMG)-driven musculoskeletal model for volitional control of a robotic ankle-foot prosthesis. This controller places the user in continuous control of the device, allowing them to freely manipulate the prosthesis behavior at will. The Hill-type muscle model was used to model a dorsiflexor and a plantarflexor, which functioned around a virtual ankle joint. The model parameters were determined by fitting the model prediction to the experimental data collected from an able-bodied subject. EMG signals recorded from ankle agonist and antagonist muscle pair were used to activate the virtual muscle models. This model was validated via offline simulations and real-time prosthesis control. Additionally, the feasibility of the proposed prosthesis control on assisting the user's functional tasks was demonstrated. The present control may further improve the function of robotic prosthesis for supporting versatile activities in individuals with lower-limb amputations.

EMG-driven Musculoskeletal Model for Volitional Control of a Robotic Ankle Prosthesis

by
Chinmay Sanjay Shah

A thesis submitted to the Graduate Faculty of
North Carolina State University
in partial fulfillment of the
requirements for the degree of
Master of Science

Mechanical Engineering

Raleigh, North Carolina
2021

APPROVED BY:

_____	_____
Dr. He Huang	Dr. Katherine Saul
Committee Co-Chair	Committee Co-Chair

_____
Dr. Nitin Sharma

BIOGRAPHY

Chinmay Shah pursued a master's degree in Mechanical Engineering with the department of Mechanical and Aerospace Engineering at North Carolina State University. He received his bachelor's degree in Mechanical Engineering from Vishwakarma Institute of Technology(VIT), Pune. After which he moved to the US to pursue a master's degree in mechanical engineering at NCSU. At NCSU, he spent a year and a half working at the Neuromuscular Rehabilitation Engineering Lab. His research under the guidance of Dr. He(Helen) Huang and Dr. Katherine Saul, focused on the development of a controller that would allow lower limb amputee's to volitionally control their powered prosthesis.

ACKNOWLEDGMENTS

I would like to thank several researchers and staff in the UNC/NC State Joint Department of Biomedical Engineering and the Mechanical and Aerospace Engineering Department at North Carolina State University for their key contributions to the work described here. I would like to thank Dr. He(Helen) Huang (Director, Neuromuscular Rehabilitation Engineering Laboratory) and Dr. Katherine Saul, my supervisors for guiding me through this project. I do not believe I could have gotten through my project without all your guidance and support. I would like to offer a special thanks to Dr. Varun Nalam, Dr. Ming Liu, Dr. I-Chieh Lee, Sameer Upadhye, and Dr. Xikai Tu for their support and mentorship throughout my time here at the NREL lab. Finally, I would like to thank all other members of the Neuromuscular Rehabilitation Engineering Laboratory (NREL): Bretta Fylstra, Aaron Fleming, Minhan Li, Robert Hinson, Noah Rubin, Wentao Liu, Joseph Berman, Fiona Popp, Brendan Driscoll, Aubrey Gray, Albert Dodson, Abbas Allili and Amirreza Naseri, I enjoyed my time here and got to learn a lot from all of you. I would like to acknowledge the funding sources for this study. This research was partially supported by the National Science Foundation through award 1954587.

TABLE OF CONTENTS

LIST OF TABLES

LIST OF FIGURES

CHAPTER 1 : INTRODUCTION

1.1 Motivation

Lower-limb amputation affects the ability of individuals to perform functional tasks, which severely affects the quality of life(Legro, Reiber, et al. 1999, Hagberg and Brånemark 2001). These individuals are prescribed passive prostheses which are incapable of restoring much of the biological function of the joint (Goldfarb 2013). To compensate for the lack of power and the inefficiencies of the passive device the individuals rely more on their intact leg and upper body. This causes an increase in metabolic cost of walking, decrease in walking speed, and can also lead to secondary physical conditions such as back pain, osteoarthritis, etc.(Schmalz, Blumentritt et al. 2002, Lamoth, Ainsworth et al. 2010, Mengelkoch, Kahle et al. 2017). To overcome this problem considerable advancements have been made in the field of robotic prosthesis enabling the development of lightweight, powered prostheses that are capable of generating similar torque and power as that of an able-bodied joint (Au, Berniker et al. 2008, Sup, Varol et al. 2009, Goldfarb 2013, Liu, Zhang et al. 2014, Lenzi, Cempini et al. 2018). These devices use a finite state controller where the task being performed is divided into various states and as the user passes through these states the device is commanded to perform the appropriate action. These controllers are autonomous; meaning they do not incorporate any form of human input into the control algorithm. They rely on the interaction of the device with the environment to identify the user's locomotion state and execute a preprogrammed set of instructions to perform the cyclic locomotion task(Varol, Sup et al. 2010, Liu, Zhang et al. 2014). Thus, new prosthesis behavior (i.e., not already pre-programmed) cannot be generated by the user to adapt to ever-changing environments (e.g., standing at a crowded bus stop, pushing a lawnmower, playing soccer, etc.).

The real world poses many uncertainties present in the environment in the form of terrain variations, obstacles, etc. Such uncertainties require spontaneous responses from the user to adapt to these changes. The lack of active control of the prosthetic ankle joint leads to poorer stability and balance confidence. This lack of balance confidence and absence of human intent from these autonomous controllers has been a hindrance to these prostheses being used in the real world.

EMG control has seen a lot of popularity recently as a method for volitional control of lower limb prostheses (Fleming, Stafford et al. 2021). The addition of human intent to these controllers has the potential to allow amputees to modulate their prosthesis mechanics, allowing them to react to the uncertainties, and volitionally perform non-repetitive tasks. Two popular methods use EMG control: Supervisory EMG control and Direct EMG control. Supervisory control is a form of discrete control where a pattern classifier is used to identify human intent by selecting the appropriate type of locomotion mode (Huang, Kuiken et al. 2009, Huang, Zhang et al. 2011). This type of control requires a significant amount of training data from the user of the device to train the pattern classifiers. But this method is prone to classification errors, where the selection of the wrong locomotion mode may lead to walking instability in prosthesis users. Continuous EMG control is another method used where the EMG signal is directly related to the force generated by the muscle. This type of continuous volitional control mimics the biological musculoskeletal systems and places the human in direct control making reactionary and non-cyclic tasks possible.

While direct EMG control can restore the ability to adapt to various environments it's unclear whether amputees can coordinate residual muscle activations to reproduce normative ankle joint function. Recent studies have shown that with appropriate training transtibial amputees can regain considerable coordination of voluntary residual muscle activity (Fleming, Huang et al.

2021). These studies have also evaluated the ability of amputee individuals to use this proportional myoelectric control to perform typical daily-life tasks and balancing tasks (Fleming and Huang 2019, Fleming, Huang et al. 2021). They implemented proportional myoelectric control on an ankle prosthesis where the muscle behavior was achieved using pneumatic artificial muscles also known as McKibben actuators. The pneumatic actuators modeled muscle behavior while the proportional EMG relayed the human intent to the system. Though this type of control has shown tremendous success, due to the presence of pneumatic actuators which require compressed air to function, this device has been constrained to laboratory testing only.

MSK model-based controllers have been applied to lower limb prosthesis control previously, these virtual muscle models capture the adaptability of the muscle to generate force depending on the state of the muscle, but they lack volitional (or EMG) control from the user. These studies have shown the capability of MSK model-based controllers to adapt to walking speeds, incline decline walking(Eilenberg, Geyer et al. 2010), and also stair climbing and stair descent (Tahir, Hessel et al. 2018). Though these MSK controllers are more adaptable than other autonomous controllers, they are limited to locomotion tasks only due to the lack of any form of human input. EMG-driven MSK model has been successfully implemented in upper-limb prosthesis control (Crouch and Huang 2016, Pan, Crouch et al. 2018). However, we are unaware of an EMG-driven MSK controller for motorized lower-limb prosthesis control. The goal of this study was to design an EMG-driven musculoskeletal (MSK) model for continuous volitional control of robotic ankle prosthesis.

1.2 Research Proposal

Autonomous controllers have been widely used to date to control powered prosthetic devices. They have enabled these devices to mimic biological similar motion during various tasks that they are programmed for. But these controllers are not effective in the presence of unknown disturbances and due to the lack of human input they are constrained to cyclic locomotion tasks. We propose replacing autonomous control with the human at the highest level of control. This will enable the controller to exploit the intelligence and adaptability of human beings in performing non-cyclic and unpredictable task. The EMG signal from the tibialis anterior muscle and gastrocnemius muscle can be used to relay the human input and place them in direct control of their device. This input will be used to drive a virtual muscle model used to predict the ankle torque generated by the muscle around the ankle joint. Building this system will allow us to virtually mimic the human neuromuscular system. The goal of this study is to

1) Develop a new EMG-driven MSK model to determine the ankle joint torque based on EMG signals from the *tibialis anterior* and the *gastrocnemius* muscles.

2) Successfully implement the control on a motorized robotic ankle prosthesis.

3) Evaluate the feasibility of our proposed control to assist with daily activities that do not include cyclic, predictive motion in the ankle.

The following chapters describe in detail the methodology, results, and evaluation in detail. Chapter 2 introduces the methodology of the MSK design and evaluation procedure. Chapter 3 describes the results for the offline simulations and real-time performance evaluation of the EMG-driven MSK model. Chapter 4 discusses the results for these evaluations, the limitations, and the future scope of this work.

CHAPTER 2 : METHODS

2.1 Control Layout

In this paper, we propose an EMG-driven MSK model-based controller where we use the EMG from the *tibialis anterior (TA)* and *medial gastrocnemius (GAS)* to activate a pair of antagonistic virtual muscles, modeled after the antagonistic muscles present around the ankle joint. While several muscles contribute to the ankle flexion moment in the sagittal plane. To develop a model that includes all those muscles we would have to develop a highly complex model which would require many parameters. Also, every modeled muscle would require its own muscle activation input which means the control would require multiple EMG inputs from multiple muscles(Crouch and Huang 2016). Thus, we modeled the virtual muscles as a lumped parameter model, where one muscle was used to represent the combined effect of multiple muscles (as shown in Fig 2.1) responsible for generating the required force. The virtual muscle was modeled as a Hill-Type muscle actuator which is a unidirectional actuator. This meant we required at least 2 virtual muscles to replicate the movement of the ankle in both the plantarflexion and dorsiflexion direction.

The force generated by the virtual muscle model was used to calculate the torque generated by the muscle around the joint. To enable us to do that we used musculoskeletal geometry which defines how the muscles interact with the skeleton and where it attaches to the skeleton. Using that relation, we were able to calculate the moment arm of the muscle as a function of the joint angle. The torque generated at the ankle joint was given by the force generated by the muscle multiplied with the moment arm of the virtual muscle (explained in detail in sections 2.3 and 2.4).

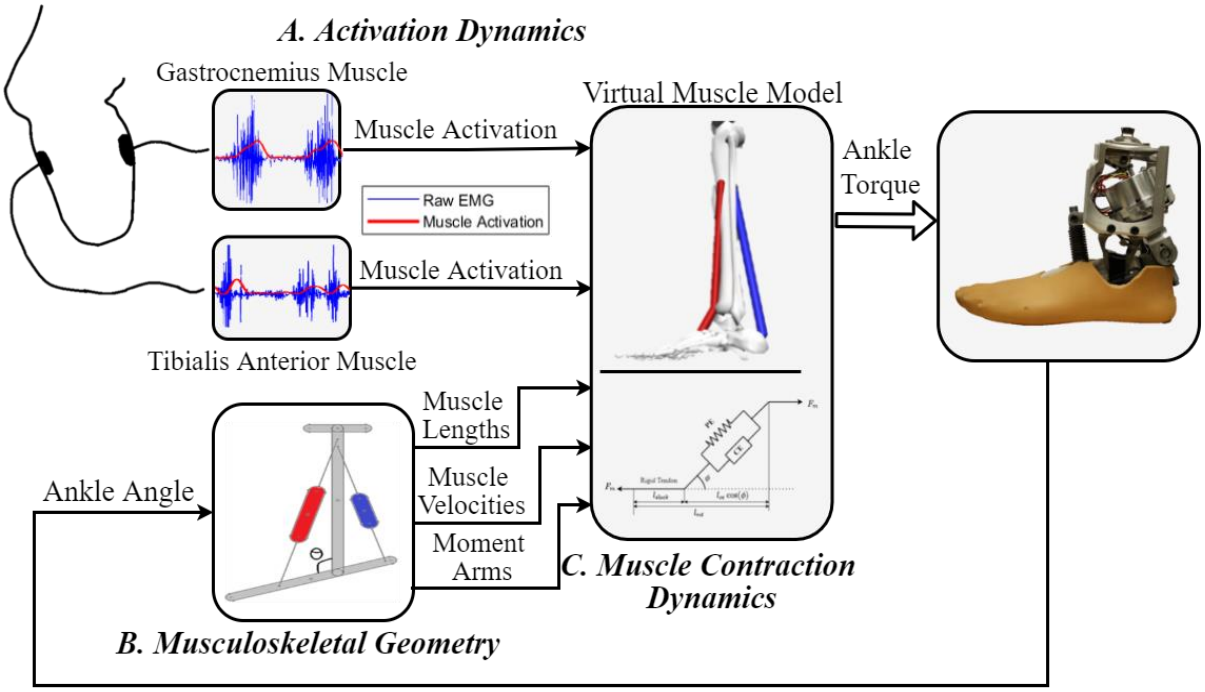

Figure 2.1 EMG-driven MSK model-based controller layout and model components - A. Activation Dynamics (EMG to muscle activation) B. Musculoskeletal Geometry, C. Muscle Contraction Dynamics.

The total joint torque was calculated by combining the effect of both the virtual muscles present in the system. During real-time control, this predicted ankle torque was sent as the reference torque command to the *VSeM* robotic ankle prosthesis(Upadhye, Shah et al. 2021). Fig. 2.1 depicts the control layout with the important parts of the EMG-driven MSK model, section 2.2. Activation Dynamics – this part deals with the signal processing of the raw EMG signal to muscle activation which is used as an input to the muscle model. Section 2.3. Musculoskeletal Geometry – this part describes how the muscle interacts with the skeleton and how the force is transferred to the joint from the muscle, and section 2.4. Muscle Contraction Dynamics – this part describes the virtual muscle model force-generating properties. The further sections describe in detail the development of the above-mentioned three components.

2.2 Activation Dynamics (EMG to Muscle Activation)

2.2.1 EMG processing

For real-time control, we placed bipolar EMG electrodes (Motion Lab Systems, MA 400) on the *TA* and *GAS*. We then high pass filtered (cutoff at 40Hz, 4th Order Butterworth) the signal to get rid of any motion artifacts. After filtering the EMG signal, it was rectified before moving on to the next step. To generate the EMG envelope, we implemented a moving average function with a 100ms sliding window on the rectified EMG signal.

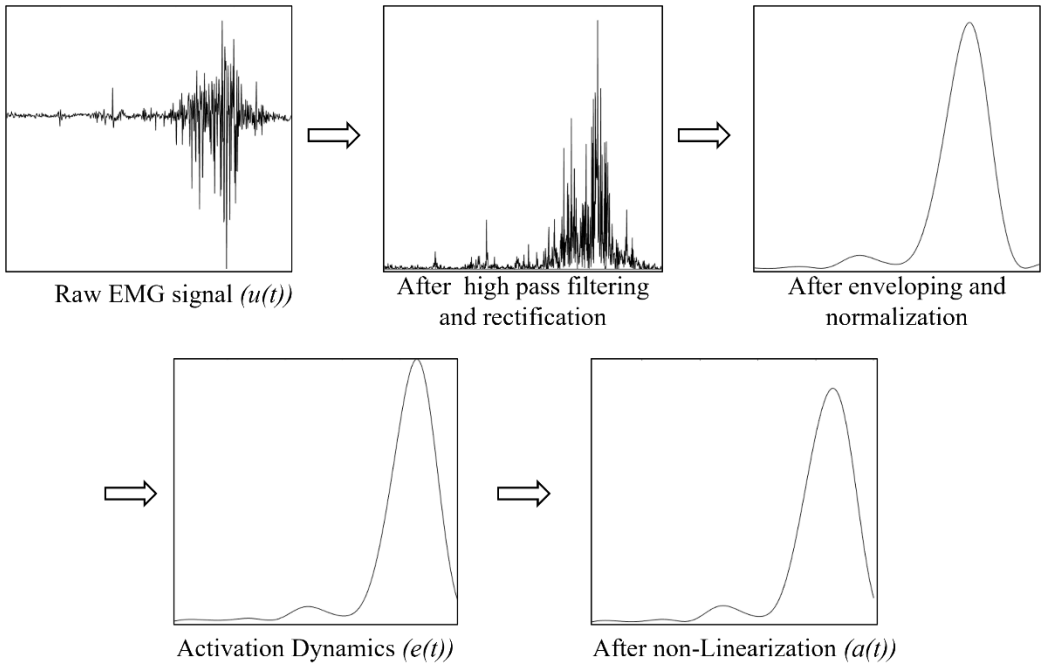

Figure 2.2 Steps involved in extracting muscle activation from raw EMG signal – High pass filtering, rectification, extracting envelope, normalization, activation dynamics and non-linearization.

The resulting signal was normalized using the max signal values obtained during the beginning of the session. To collect the max signal values, the participant was asked to flex each muscle maximally three times. We took the max value as the average of the three generated peaks.

This process was performed quite carefully, as the entire model predictions are quite sensitive to this normalization. An error in the maximum signal values could cause an error with the normalization, which could lead to muscle activations above a unit value. In that case, the muscle model might predict forces above the maximum isometric force that the muscle can generate. Fig 2.2 depicts the processes performed on the raw EMG signal to generate the corresponding muscle activation signal.

2.2.2 Activation Dynamics

We used this rectified, normalized, and enveloped EMG $(e(t))$ signal to calculate the corresponding neural activation $(u(t))$[1]. In the human neuromuscular system, the muscle fiber is activated by a single action potential which is results in a twitch response of the muscle fiber. This response corresponds to the neural activation signal. That response is a result of a chemical reaction taking place in the muscle which can be represented as a critically damped second-order differential system. The following equation captures the relationship between neural activation $(u(t))$ and EMG input $(e(t))$ (Buchanan, Lloyd et al. 2004).

$$u(t) = M\frac{de^2(t)}{dt^2} + B\frac{de(t)}{dt} + Ke(t) \quad (1)$$

Since we sample EMG data at discrete time intervals. We used a discrete version of the above mentioned second-order differential equation to represent the relation between EMG and neural activation(Lloyd and Besier 2003, Buchanan, Lloyd et al. 2004),

[1] Nomenclature defined in Appendix A

$$u(t) = \alpha\, e(t-d) - \beta_1\, u(t-1) - \beta_2\, u(t-2) \quad (2)$$

where $\alpha = 0.9486$, $\beta_1 = -0.056$ & $\beta_2 = 0.000627$ (Lloyd and Besier 2003). This equation is also seen as a recursive filter as the current value of neural activation depends on the previous two values as well i.e., its recent history. d represents the electromechanical delay (a time delay) present between the onset of the EMG signal and the contraction of the muscle to generate force. In literature, this delay has been reported to be in the 10-100msec range (Corcos, Gottlieb et al. 1992). This delay is mainly generated due to 2 factors, (i) the time taken to transport the calcium ions across the membrane, and the muscle fiber conduction velocities, and (ii) dynamics of force production which depends on chemical dynamics of the muscle depolarization and muscle contraction dynamics (Corcos, Gottlieb et al. 1992).This delay was determined based on the experimental data collected for the training of the model for offline simulations and further tuned for real-time control corresponding to the delay present in the robotic ankle prosthesis.

This neural activation cannot be directly used as muscle activation i.e., input to the virtual muscle model. At lower levels of force, this neural activation has a non-linear relationship with muscle activation. This relationship was captured by the given equation (Lloyd and Besier 2003).

$$a(t) = \frac{e^{Au(t)} - 1}{e^{A} - 1} \quad (3)$$

where A represents the non-linear shape factor, which is constrained between, $-3 < A < 0$. $a(t)$ represents the final input that was sent to the virtual muscle model as muscle activation.

2.3 Musculoskeletal Geometry

The musculoskeletal geometry defines how the muscle attaches i.e., interacts with the skeleton and hence the environment. It is used to identify the relationship between the change in

length of the moment arm with the change in joint angle. As the joint torque produced is the product of the muscle force and the moment arm, $\tau_m = r(\theta)F_m$.

This variable moment arm r is a function of joint angle (θ) and it's relation was given by the following equation (Geyer and Herr 2010).

$$r(\theta) = r_{max}\, cos(\theta - \theta_{max}) \tag{4}$$

where r_{max} is the maximum moment arm length and θ_{max} was defined as the angle at which, the moment arm is maximum in length (Fig 2.3).

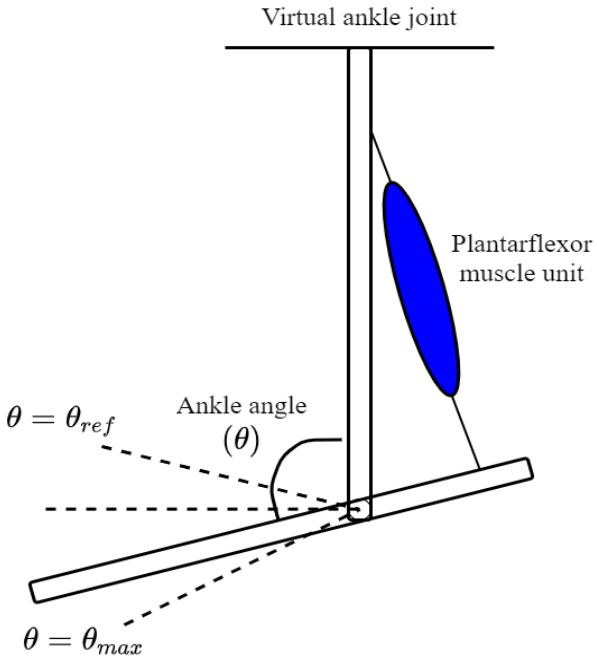

Figure 2.3 The musculoskeletal geometry of the plantarflexor muscle unit in the virtual ankle model.

θ is the ankle joint angle measured between the shank and the foot (as shown in Fig 2.3). This angle was measured using the encoder built into the ankle prosthesis when the control was implemented in real-time on the robotic ankle prosthesis. The two angles θ_{max} and θ_{ref} were the

reference angles at which length of the muscle unit and moment arm length were known, they were used as a reference to calculate the length at different joint angles. The length of the muscle unit as mentioned before is a function of the joint angle, it was computed using the following relation (Geyer and Herr 2010).

$$l_{mt} = l_o \cos(\phi_{ref}) + l_{slack} - r \sin(\theta_{max} - \theta_{ref}) + r \sin(\theta_{max} - \theta) \quad (5)$$

where l_{mt} is the length of the muscle unit (Fig 2.4), which is defined as the length of the entire muscle between the attachment points. l_o is the optimal muscle fiber length, which is the length of the muscle fiber when the muscle generates peak force.

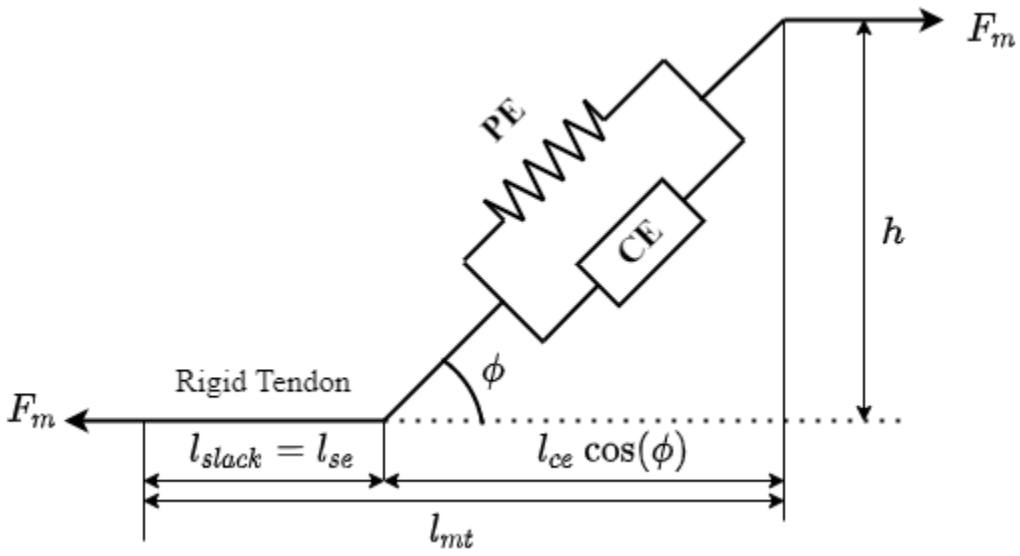

Figure 2.4 Hill-Type muscle model considered in this study, consisting of a contractile element (force-generating element), parallel elastic element and a rigid tendon.

l_{slack} represents the slack length of the tendon unit in the muscle model. θ_{ref}, ϕ_{ref} are the ankle angle and pennation angle respectively, when the muscle fiber length (l_{ce}) (Fig 2.4) is equal to the optimal muscle fiber length (l_o).

The length of the muscle model as seen in Fig 2.4, can also be expressed as the sum of contractile element length (muscle fiber length) and series elastic element(tendon) length.

$$l_{mt} = l_{ce}\cos(\phi) + l_{se} \tag{6}$$

Since a rigid tendon model was assumed, the length of the tendon/series elastic element does not change i.e., $l_{slack} = l_{se}$. This slightly reduces the prediction accuracy of the model but helps to reduce the complexity of the problem (Millard, Uchida et al. 2013).

As seen in Fig 2.4 the pennation angle is the angle at which the muscle fibers attach to the series elastic element. The pennation angle, ϕ, is not constant and changes with the length of the muscle unit. The assumption was made that the muscle fibers maintain a constant thickness and volume during muscle contraction (Lloyd and Besier 2003). Which implies that h (as seen in Fig 2.4) remains constant. This assumption was used to calculate the pennation angle at any instant as a function of the length of the muscle fiber.

$$l_o\, sin(\phi_{ref}) = h \tag{7}$$

$$l_{ce}\, sin(\phi) = h \tag{8}$$

Form Eq. 7 and Eq. 8 we can derive the following equation.

$$\phi(t) = sin^{-1}\left(\frac{l_o \sin(\phi_{ref})}{l_{ce}}\right) \tag{9}$$

Eq 5, 6, and 9 were used to compute l_{ce} length of the contractile element which is one of the inputs to the muscle model.

Assuming a rigid tendon model, simplified the (v_{ce}) velocity of contraction calculations. By differentiating Eq 6 and 7 with respect to time we obtained the following relation (Millard, Uchida et al. 2013).

$$v_{mt} = \dot{l_{mt}} = -r\,cos(\theta_{max} - \theta)\,\dot{\theta} \tag{10}$$

where $\dot{\theta}$ is the ankle speed calculated by numerically differentiating the ankle angle data collected from the encoder in real-time.

$$v_{mt} = \dot{l_{mt}} = \dot{l_{ce}}\,cos(\phi) - l_{ce}\,sin(\phi)\;\dot{\phi} \tag{11}$$

where $\dot{\phi}$ can be derived from differentiating Eq 8 with respect to time,

$$\dot{l_{ce}}\sin(\phi) + l_{ce}\;\dot{\phi}\;cos(\phi) = 0 \tag{12}$$

$$\dot{\phi} = \frac{-\dot{l_{ce}}\,sin(\phi)}{l_{ce}\,cos(\phi)} \tag{13}$$

using Eq 11 and 13 we derive the following relation

$$v_{ce} = \dot{l_{ce}} = v_{mt}\,cos(\phi) \tag{14}$$

The above equation enabled us to calculate the velocity of contraction v_{ce} which is the final input to the muscle model.

2.4 Muscle Contraction Dynamics

The lumped parameter models were developed by considering them as hill-type muscle models(Archibald 1938, Hill 1938, Vivian 1938, Zajac 1989, Winters 1990). As seen in Fig 2.4 the Hill-type muscle model consists of an active contractile element (responsible for generating the force) which represents the muscle fibers, a parallel passive element which represents the elastic tissue around the muscle fibers , and a series elastic element which represents the tendon. As a rigid tendon assumption was made, the series elastic element was not included in the model. The muscle model as mentioned before consisted of 2 muscles one representing the plantarflexor muscles and the other representing the dorsiflexor muscles (Fig 2.5). Since the hill-type muscle

model is a unidirectional actuator the contribution of both the muscles were needed to generate the required torque and motion in both direction in the sagittal plane. The entire unit (contractile element, parallel elastic element and rigid tendon) is referred to as the muscle unit.

2.4.1 Active Contractile Element

Force generated by the human muscle is dependent on the change in muscle fibre length (l_{ce}) and velocity of contraction (v_{ce}) (Hill 1938, Zajac 1989, Winters 1990). The total force generated by the active contractile element (F_{ce}) is a function of l_{ce}, v_{ce} and a which represent the length of the contractile element, the velocity of contraction, and muscle activation respectively.

$$F_{ce} = F_{max} F_l(l_{ce}) F_v(v_{ce}) a \tag{15}$$

F_{max} represents the maximum isometric force generated by the muscle. $F_l(l_{ce})$ represents the force-length relationship for a Hill-type muscle model, represented by a bell-shaped curve described by the following equation(Geyer and Seyfarth 2016),

$$F_l(l_{ce}) = e^{\frac{-(l_o - l_{ce})^2}{(l_o w)^2}} \tag{16}$$

w was fixed to a value of 0.56 (Geyer and Seyfarth 2016), this parameter adjusts the width of the bell-shaped curve representing the force-length behavior of the muscle model.

$F_v(v_{ce})$ represents the dimensionless force-velocity relationship for a hill-type muscle model, which is described by the following equation,

$$F_v(v_{ce}) = \begin{cases} \dfrac{v_{max} - v_{ce}}{v_{max} + K v_{ce}}, v_{ce} < 0 \\ N + (N-1)\dfrac{v_{max} + v_{ce}}{7.56 K v_{ce} - v_{max}}, v_{ce} \geq 0 \end{cases} \tag{17}$$

In Eq 17. v_{max} represents the maximum contraction velocity of the muscle fiber which was set to 10 $\frac{l_o}{s}$ (Hill 1938, Zajac 1989, Winters 1990). K is the shape parameter fixed to 5 (Geyer and Seyfarth 2016) and N is a dimensionless force constant fixed at 1.5 (Geyer and Seyfarth 2016). All of these parameters that define the dynamic force-length and force-velocity relations of the muscle are summarized in Table 2.1.

Table 2.1 Muscle model parameter fixed for all muscles.

Parameters	***Value***
w	0.56
$\boldsymbol{v_{max}}$ $(\frac{l_o}{s})$	10
K	5
N	1.5
$\boldsymbol{\epsilon_{pe}}$	0.56

2.4.2 Parallel Elastic Element

The parallel elastic element present in the system only contributes to force generation if the muscle fibers are stretched beyond the optimal fiber length l_o (Geyer and Seyfarth 2016). This is part represents the elastic behavior of the tissues present around the muscle fibers,

$$F_{pe} = F_{max}\left(\frac{l_{ce} - l_o}{l_o \epsilon_{pe}}\right)^2, l_{ce} > l_o \tag{18}$$

In Eq 19. ϵ_{pe} is the reference strain which is fixed at 0.56 (Geyer and Seyfarth 2016).

2.4.3 Muscle Interaction

The total force generated by the muscle unit (F_m) is a combination of the force generated by the active and passive elements. This force is transmitted at an angle(the pennation angle) as the muscle fibers are not in-line with the tendon(as shown in Fig 2.4). The total force is given by

$$F_m = \left(F_{ce} + F_{pe}\right)\cos(\phi) \tag{19}$$

where F_{ce} represents the force generated by the contractile element and F_{pe} denotes the force generated by the parallel elastic element.

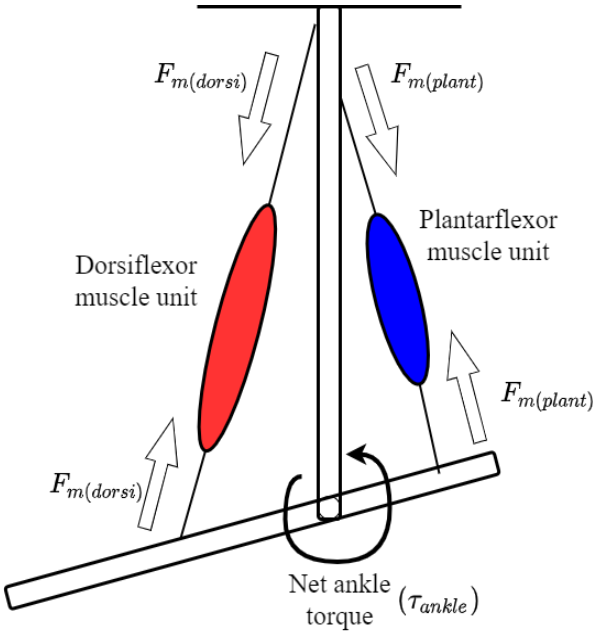

Figure 2.5 Virtual ankle muscle attachment and loading diagram. The diagram represents the force generated by the dorsiflexor muscle unit $F_{m(dorsi)}$, plantarflexor muscle unit $F_{m(plant)}$ and the combined ankle torque generated at the ankle (τ_{ankle}).

The force generated by the muscle unit when combined with information calculated using the musculoskeletal geometry enabled us to calculate the corresponding ankle torque as shown in

Fig 2.5. The amount of torque generated by the muscle depends on the muscle force but also the moment arm corresponding to the joint angle.

$$\tau_m = F_m\, r(\theta) \tag{20}$$

Combining all of the equations, the net ankle joint torque was computed by summing the torque contribution of the 2 muscles present in the model as seen in Fig 2.3,

$$\tau_{ankle} = F_{m(dorsi)} r_{dorsi}(\theta) \; - \; F_{m(plant)} r_{plant}(\theta) \tag{21}$$

where τ_{ankle} represents the model predicted ankle torque. This calculated ankle torque was sent to the robotic ankle prosthesis as the reference torque command.

2.5 Model Parameter Determination

The EMG-driven MSK model consists of many parameters that enable it to replicate the dynamic force-generating behavior of muscles. Some of these parameters are fixed to preserve this dynamic force-length, force-velocity relationship – these parameters were chosen from literature. Other parameters are responsible for scaling the muscle force according to the individual muscles present in the body. The optimization problem was set up to find a set of these physiological parameters that would allow the muscle model predictions to best fit the biological ankle torque collected during walking tasks (at various speeds). F_{max}, l_o, r_{max}, θ_{ref}, θ_{max} were the physiological parameters chosen for optimization. θ_{ref} and θ_{max} are the musculoskeletal geometry related parameters which were shared by both the muscles. θ_{ref} is defined as the ankle angle at which the length of the muscle fibers is equal to the optimal muscle fiber length and θ_{max} is the ankle angle at which the moment arm is maximum length. Since the length of the muscle and moment arm is known at these two reference angles, the length of the muscle unit can be calculated at other angles using these values as reference.

2.5.1 Optimized Parameters

The following physiological parameters were chosen to be tuned- F_{max}, l_o, r_{max}, θ_{ref}, θ_{max}. MATLAB's built-in *GlobalSearch* function was recruited to perform the optimization(Crouch and Huang 2016). Table 2.2 enlists the optimizer settings chosen to perform the optimization. The biological ankle torque generated by the muscle at the ankle joint collected during three treadmill walking speeds – 1.0m/s, 1.2m's and 1.4m/s were chosen to perform the optimization. The data from all of these trails was combined to perform the optimization. The EMG signals form the *TA* muscle, *GAS* muscle and the corresponding ankle angle data collected during treadmill walking were chosen as the inputs to the model during optimization. These inputs

Table 2.2 *GlobalSearch* optimization algorithm settings.

Fmincon	"MaxIter"	8000
Solver	"MaxFunEvals"	8000
Settings	"TolFun"	0.01
GlobalSearch Settings	"NumTrialPoints"	700

Table 2.3 Allowable ranges for numerical optimization of chosen parameters.

Model Parameter	***Min Value***	***Max Value***
Plantar flexor		
F_{max} ***(N)***	500	6000
l_o ***(m)***	0.02	0.06
r_{max}***(m)***	0.01	0.065
Dorsi flexor		
F_{max} ***(N)***	500	4000
l_o ***(m)***	0.02	0.145
r_{max} ***(m)***	0.01	0.065
θ_{ref} ***(deg)***	70	130
θ_{max}***(deg)***	70	130

enable the model to calculate the corresponding muscle activations, muscle lengths, velocity of contraction and moment arms hence the ankle torque. The allowable ranges of the chosen parameters for optimization can be seen in Table 2.3.

2.5.2 Target Behavior

Biological kinematic and kinetic data was collected during walking at various speeds to calculate the biological ankle torque generated by the muscle at the ankle joint. This trajectory was used as the target values for optimizing the model and determining the model parameters. We recruited one able-bodied participant (175cm height and 75kg weight) for the study with IRB approval and signed informed consent. To build and validate a subject-specific model, bipolar EMG electrodes were placed on the *TA* and *GAS* to collect the raw EMG data from these specific muscles. The muscles were located by palpation and visualizing the EMG signal before the data collection.

To capture the kinematics of the subject, retroreflective markers were placed on the subject. A 12-camera motion capture system (Vicon, UK) was used to track the marker positions at 100 Hz. The markers were placed at 16 locations on the subject according to the lower body template(plugin gait lower body ai) inbuilt into the Vicon software.

The ground reaction forces were measured at 1000 Hz using a split-belt instrumented treadmill (Bertec, USA). The participant was asked to walk on the treadmill at various speeds - 1.0m/s, 1.2m/s, and 1.4m/s for 2 minutes each.

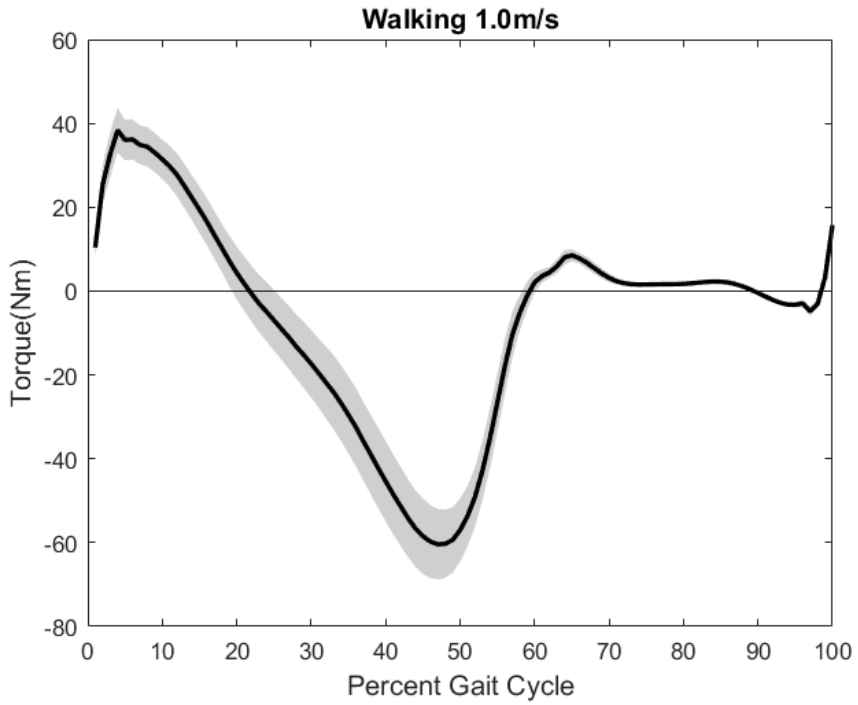

Figure 2.6 Ankle torque trajectory(Black line) while walking a 1.0m/s for recruited participant. Shaded region represents the +/- one standard deviation, +ve torque values represent dorsiflexion torque and -ve values represent plantarflexion torque.

Inverse dynamics was performed on the ground reaction force data and joint kinematics collected from the motion capture system to calculate the torque generated at the ankle joint by the muscles during walking. Figs 2.6 and 2.7 show the biological ankle joint torque trajectory averaged across the gait cycle calculated from the data collected during these trials which are used as the target behavior for the model optimization. The EMG signals, ankle angle, and calculated ankle torque during walking tasks were used to establish the MSK model parameters via optimization as discussed in the previous section.

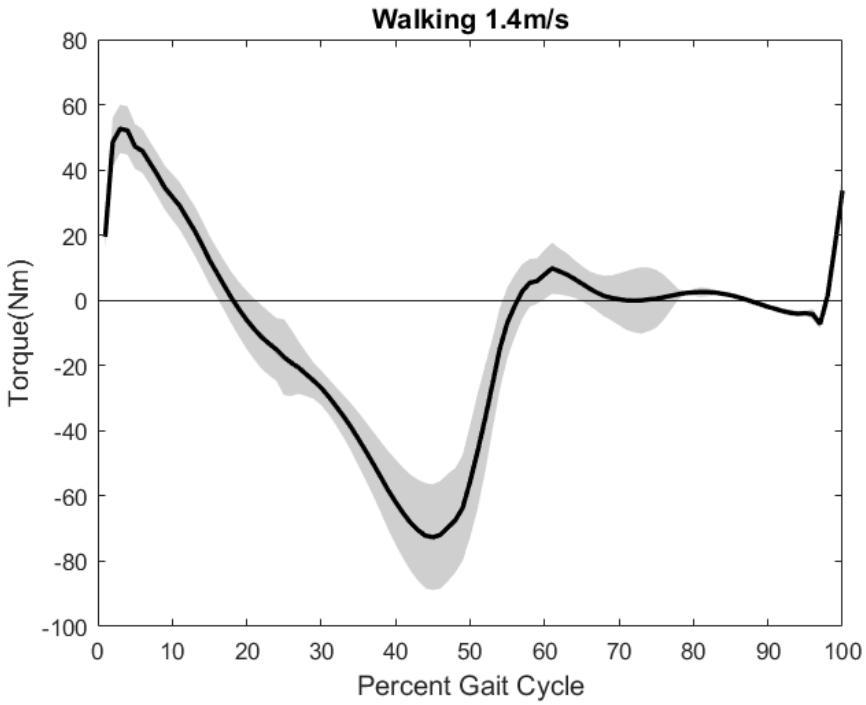

Figure 2.7 Ankle torque trajectory(Black line) while walking a 1.4m/s for recruited participant. Shaded region represents the +/- one standard deviation, +ve torque values represent dorsiflexion torque and -ve values represent plantarflexion torque.

2.5.3 Cost Function

The goal of this optimization function was to minimize the sum of squared error between the model predicted ankle torque τ_{ankle} and biological ankle torque τ_{bio} collected during the walking trials shown in Fig 2.6 and 2.7 during various walking speeds, where the error was given by,

$$error = \frac{1}{n}\sum_{1}^{n}(\tau_{ankle} - \tau_{bio})^2 \tag{22}$$

n is the length of data used in optimization.

2.6 Real-Time Implementation

The EMG model-based controller developed here was implemented in real time on the *VSeM* robotic ankle prosthesis (Fig.2.8) developed at the Neuromuscular Rehabilitation Engineering Lab at NCSU (Upadhye, Shah et al. 2021). The device is capable of producing a peak torque of 139Nm and is equipped with an adjustable parallel elastic element. The parallel element comprises of Belleville disc springs that can be added or removed to adjust the stiffness, equilibrium point and range of motion.

The model-based controller was implemented in real-time using the TwinCAT 3.1 (Beckhoff Automation GmbH, Germany) using a C++ versioned driver on a Windows 10 Desktop. This control platform developed provided a user-friendly setup where the changes to the model could be quickly implemented and evaluated, it has a quick debugging system inbuilt that allowed

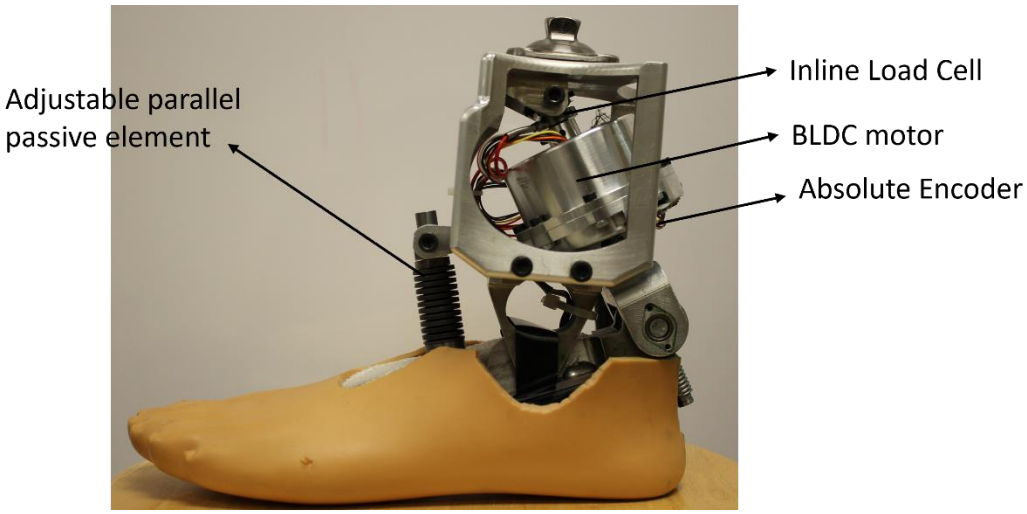

Figure 2.8 *VSeM* robotic ankle Prosthesis.

for online debugging of the control code. Here the EtherCAT(Ethernet for Control and Automation Technology) communication protocol was utilized to establish communication between the controller, data acquisition devices(load cell) and motor driver. Over other standard Fieldbus systems such as CAN, Profibus etc., the EtherCAT communication protocol has several

advantages such as reduced jitter, more precise clock synchronization, and higher bus cycle bandwidth, which enables cycle times in the microsecond range(Langlois, Hoeven et al. 2018). Fig 2.9 showcases the mechatronic system physically connected via the EtherCAT communication protocol to allow for real-time implementation of the EMG-driven model.

2 Bi-polar electrodes were placed on the *TA* and *GAS* muscle of the participant. The EMG-electrodes were connected to the motion lab EMG-system(Motion Lab systems MA 400), the corresponding signal cables were connected to an analog I/O module (ECAT 2011-H). All of the analog signals connected from this module were sent to the control PC.

The loadcell (LCM systems model DCE-1KN) present in the ankle prosthesis as shown in Fig 2.8 was connected to an amplifier Tacuna Systems (model EMBSGB200-M), this amplified signal measured using the analog I/O module. The inline load cell was used to measure the prosthesis generated torque during real-time implementation of the control.

The ankle angle was measured using the motor encoder motor encoder (Renishaw RLS model MB064DCC18MDDA00) present in the system. The ankle angle and EMG signals together formed the inputs to the virtual muscle model. The I/O module was connected to the motor driver (ELMO motion control Gold Solo twitter drive) and the Windows 10 control PC via inexpensive RJ 45 ethernet cable. All of these control signals were relayed to the control PC and fed into the virtual muscle model coded in C++. The ankle torque predicted by the muscle model was converted to the corresponding motor torque command.

This command was sent to the motor driver connected to the Brushless DC motor present in the robotic ankle prosthesis. The I/O module and Elmo Gold Twitter are powered by a 24 V, 42A power source (Ampflow Model S-1000-24), while the load cell amplifiers are powered using standard 9V PP3 batteries. The entire system was running at a sampling rate of 1000Hz.

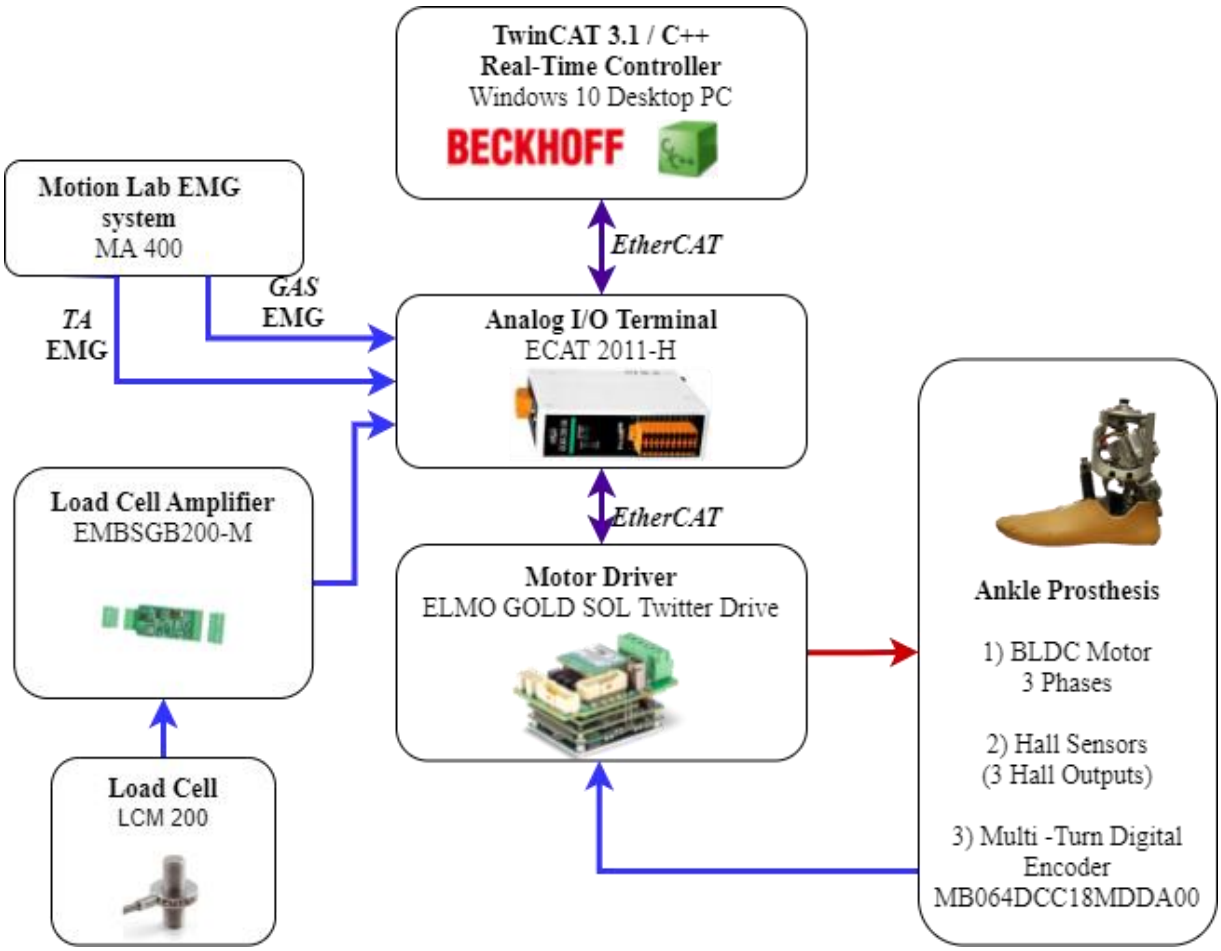

Figure 2.9 Mechatronic system layout – (blue lines) indicate inputs, (red line) output and (purple line) EtherCAT communication protocol connections.

As mentioned in the above sections the real-time control was divided into components that played specific roles in the implementation of this EMG-driven model. Activation dynamics performed digital signal processing (as described in section 2.2) on the raw EMG signal and calculated the corresponding *GAS* and *TA* activations. The ankle angle was used to calculate the corresponding moment arms, muscle lengths and muscle contraction velocity (as described in section 2.3). All of these processed signals were fed into the virtual muscle model which was used to calculate the net ankle joint torque. The predicted ankle joint torque was transformed into the

motor current command. This motor current command was sent to the motor driver and hence the BLDC motor present in the robotic ankle prosthesis.

2.7 Evaluation Protocol

2.7.1 Data Collection Device Setup

Evaluation of our proposed EMG-driven MSK model control included three parts. In the first part, we conducted an offline evaluation of the EMG-driven MSK model for predicting the ankle joint torque. In the remaining part of the evaluation the control was implemented in real-time on a robotic ankle prosthesis, and the feasibility of the real-time control was evaluated.

As we have created a subject specific model, we recruited the same able-bodied participant (175cm height and 75kg weight) for the evaluation part of the study with IRB approval and signed informed consent. To capture the kinematics of the subject, retroreflective markers were placed on the subject. A 12-camera motion capture system (Vicon, UK) was used to track the marker positions at 100 Hz. The markers were placed at 16 locations on the subject according to the lower body template(plugin gait lower body ai) inbuilt into the Vicon software. The ground reaction forces were measured at 1000 Hz using a split-belt instrumented treadmill (Bertec, USA). Bipolar electrodes were placed on the *TA* and *GAS* muscles to collect raw EMG data which was sampled at 1000 Hz. When the control was implemented in real-time on the device the input from the encoder was used to calculate the ankle angle, which was sent as an input to the virtual model. The inline load cell present in the device was used to measure the ankle torque generated by the prosthetic device.

a)

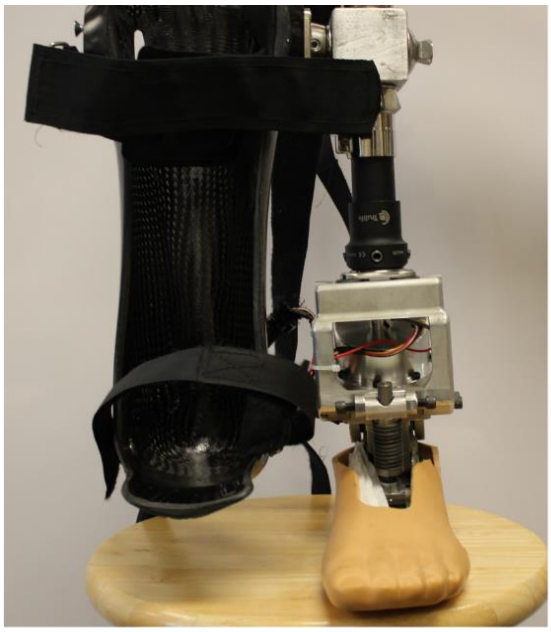

b)

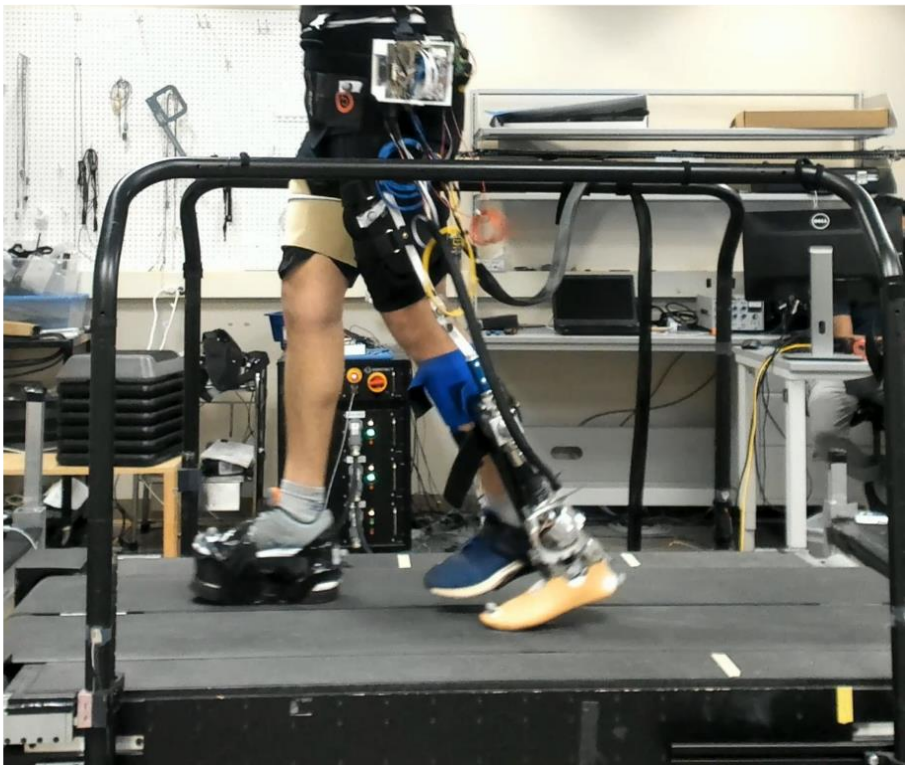

Figure 2.10 (a)Able-bodied adaptor connected to the robotic ankle prosthesis (b)Able-bodied participant wearing the device with the adaptor(Upadhye, Shah et al. 2021). (© 2021 IEEE).

2.7.2 Evaluation Protocol

Offline simulations were performed to assess the prediction accuracy of the model across various tasks with different torque ranges and ankle range of motion. For the offline simulations, the trials that were not used for training the model were used to perform those simulations. While the model was trained on walking tasks, offline simulations were performed for other tasks as well such as squatting, performing sit-to-stand transitions and sanding on their toes. The goal was to see how well the model trained on one particular task would perform while evaluating the model on different tasks with different torque requirements and ankle range of motion.

One of the most important part in every data collection session was the accurate collection of the maximum EMG signal value for normalizing the raw EMG. At the beginning of every data collection session the participant was asked to maximally activate their TA muscle by trying to dorsiflex their ankle under an applied load and the gastrocnemius muscle by trying to stand on their toes of only one side whose maximum signal values need to be recorder. This procedure was repeated three times to attain the maximum signal of each trial. The average of these maximum signal values was used to normalize the EMG signal during their processing to muscle activations.

During the real-time implementations the human ankle was attached to an able-bodied adaptor to allow able-bodied subjects to wear and operate the device (shown in Fig 2.10). Due to the inability of the subject to activate the *GAS* and *TA* individually when the foot was fixed in the adaptor, the EMG signals were recorded from the intact side. This restricted testing of the controller to only bilaterally symmetrical tasks. In the third part of the evaluation, we tested the model-based control in an open loop with non-weight bearing posture tasks (shown in Fig 2.11). The subject was asked to sit on a chair comfortably and performed ankle dorsiflexion and plantarflexion repeatedly on the intact limb. Two non-weight bearing posture tasks were performed

(Fig 2.11) a) when both the intact foot and the prosthetic foot were in the air and b) when both the feet were rested on a flat surface and the user performed plantarflexion dorsiflexion simultaneously. The EMG-driven MSK model estimated the intact ankle torque and then applied it to the prosthetic ankle.

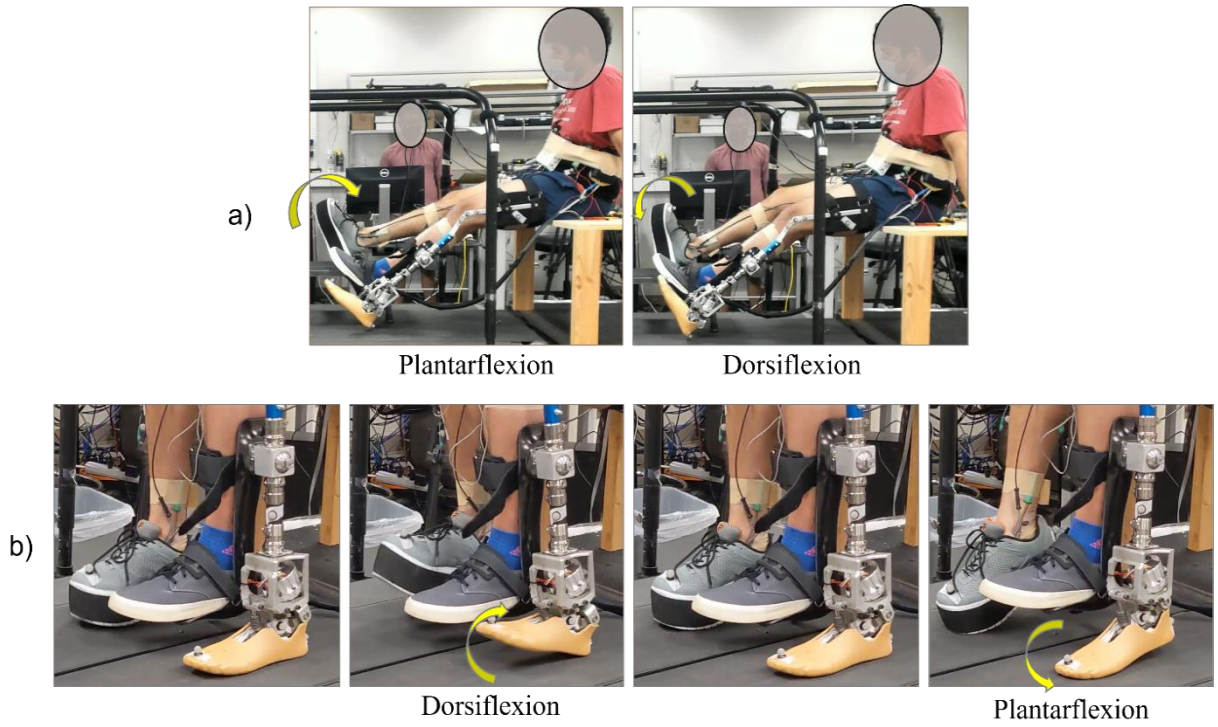

Figure 2.11 Non-weight bearing posture tasks performed by the user a) Plantarflexion-dorsiflexion when foot is in the air, b) Plantarflexion-dorsiflexion when the foot is rested on a flat surface.

In the remaining part of the evaluation, we aimed to show the feasibility of our proposed control in a closed-loop (with a human operator in the loop), using weight-bearing tasks. The tasks included standing on toes (Fig 2.12 (a)) and performing sit-to-stand transitions (Fig 2.12 (b)). These tasks were chosen as they are unpredictable and non-repetitive tasks. The measurement methods during these real-time evaluations were the same as the measurements when collecting

data for training and offline validation of the model. The prosthesis-generated ankle torque was measured using a loadcell present in the ankle prosthesis.

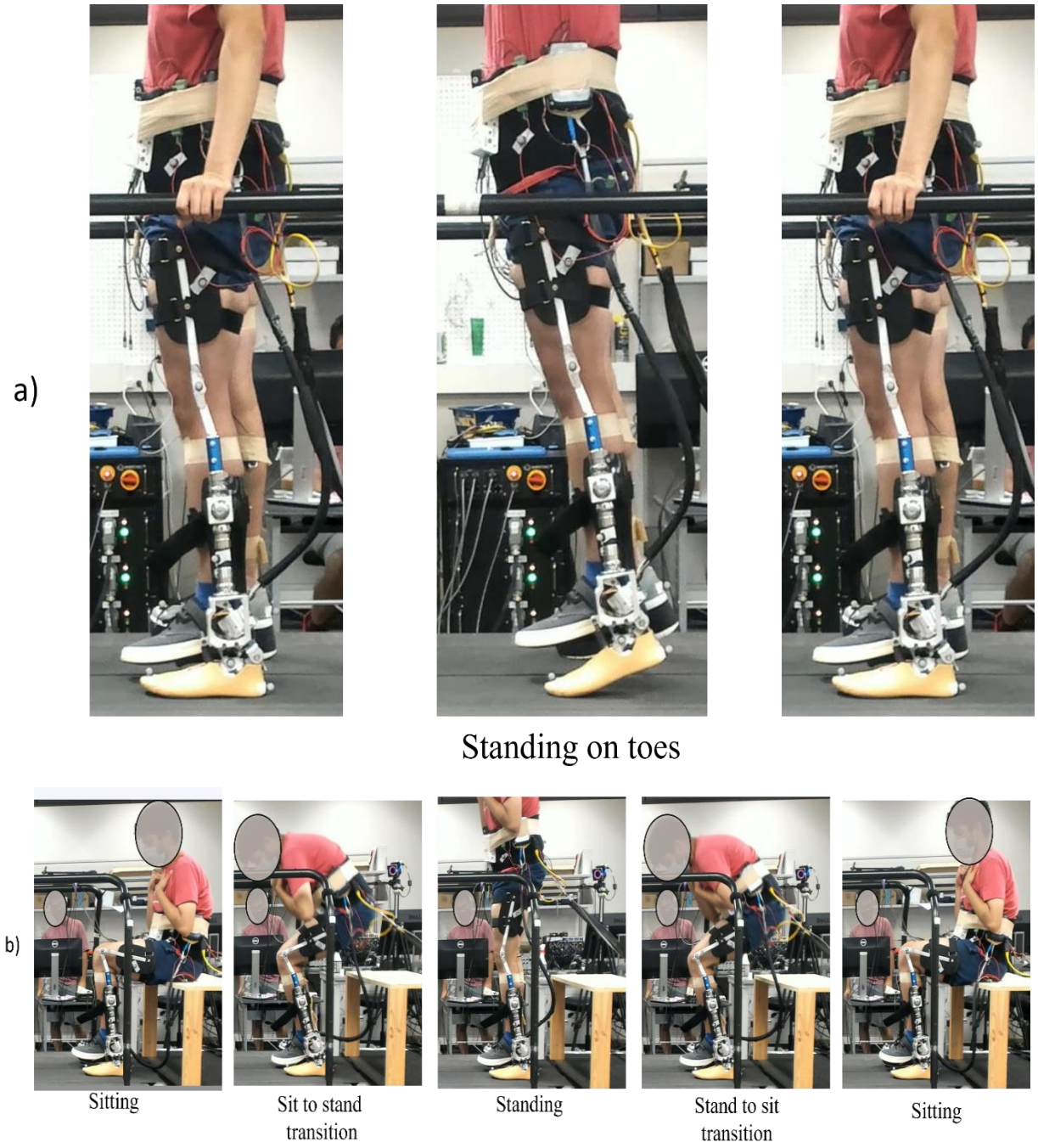

Figure 2.12 Weight bearing tasks performed by the user - a) Standing on toes task b) Sit-to-stand transitions.

2.8 Data Analysis and Evaluation Metrics

Biological ankle torque was calculated using the kinematic joint motion and ground reaction forces through an inverse dynamic model. Visual 3D (C-motion Inc., USA) was used to perform the inverse dynamics calculations. The model optimization was performed in MATLAB (Mathworks, Natick, MA). The GlobalSearch algorithm inbuilt in MATLAB was recruited to perform the optimization. The EMG data was sampled at 1000Hz while biological motion data was sampled at 100 Hz. The EMG data was resampled to be consistent to ensure a consistent sampling rate across all the inputs to the muscle model during optimization.

In the first part of the evaluation, for offline simulations we used R^2 value and Normalized Root Mean Square Error (NRMSE) values between inverse-dynamic calculated biological ankle torque and model predicted ankle torque to assess the accuracy of the MSK model predictions. Since all the tested tasks were repeated motions, we segmented each repetition, normalized the duration of each repetition as % completion of each attempt, and averaged all the repetitions across the same task.

In the remaining parts of the evaluation, NRMSE and R^2 values were calculated between the model predicted ankle torque, the ankle angle/torque of the prosthesis, and biological ankle angle/torque on the intact side.

CHAPTER 3 : RESULTS

3.1 Optimization Results

A set of parameters was obtained from performing the optimization mentioned in section 2.5.1 where the goal was to match the model prediction with the biological ankle torque. Table 3.1 summarizes the parameter values obtained from the GlobalSearch optimization.

Table 3.1 Optimization Results - Optimized Parameter Values.

Model Parameter	***Optimized Value***
Plantar flexor	
F_{max} ***(N)***	4800
l_o ***(m)***	0.0402
r_{max}***(m)***	0.0375
Dorsi flexor	
F_{max} ***(N)***	1800
l_o ***(m)***	0.065
r_{max} ***(m)***	0.0449
θ_{ref} ***(deg)***	70
θ_{max}***(deg)***	112

3.2 Offline Simulations

To verify the effectiveness of the optimization and the performance of the EMG-driven MSK model offline simulations were conducted. Here the trials that were not used for training were used to perform the cross-validations. The simulations were conducted for various different tasks – A. Treadmill walking at 1.0m/s B. Treadmill walking at 1.4m/s, C. Sit-to-stand transition, D. Standing on toes, E. Squatting. As mentioned in section 2.6.1 the EMG-data and ankle angle data was given to the model as inputs to predict the ankle torque. Fig 3.1 compares the ankle torque predicted by the EMG-driven MSK (blue dashed line) and the biological ankle torque calculated by the inverse dynamics (red solid line) for various tasks. Since these are repetitive tasks, they were averaged across the cycle and presented in the form of % completion. The shaded areas depict one standard deviation above the average ankle torque and one standard deviation below.

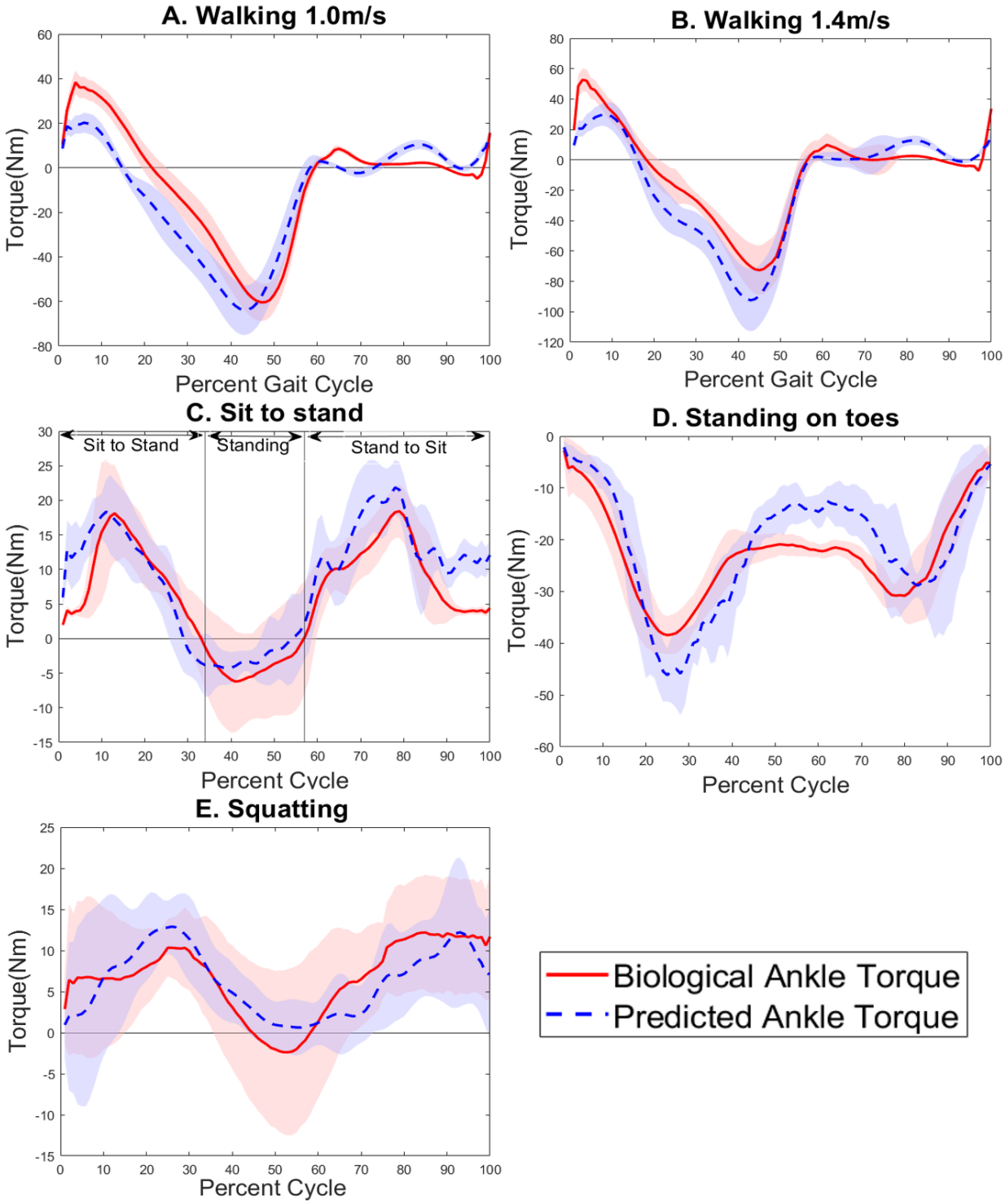

Figure 3.1 Comparison of the biological ankle torque calculated by inverse dynamics (+ve torque corresponds to dorsiflexion torque and -ve torque represents the plantarflexion torque) with MSK model predicted torque for different tasks: A. walking at 1.0 m/s, B. walking at 1.4 m/s, C. sit-to-stand transitions, D. standing on toes, E. squatting. The solid and dash data represent the averaged curve across multiple repetitions. Shaded area denotes +/- one standard deviation.

Fig 3.1 compares the model predicted torque with the biological ankle torque calculated using inverse dynamics form the biological motion data. Table 3.2 enlists the normalized root mean square error (NRMSE) and R^2 value of model predicted ankle torque with the biological ankle torque for the various tasks.

Table 3.2 Ankle torque prediction accuracy during offline simulations of EMG-driven MSK model.

	Task	***NRMSE***	***R^2***
a)	***Walking 1m/s***	0.1173	0.8210
b)	***Walking 1.4 m/s***	0.0935	0.8895
c)	***Sit to stand***	0.1695	0.7792
d)	***Standing on Toes***	0.1656	0.6842
e)	***Squatting***	0.1882	0.6205

3.3 Real-time open loop control in non-weight bearing posture tasks

This experiment was setup to study the real-time feasibility of the control when it was implemented on the robotic ankle prosthesis. The participant wore the device and performed simple non-weight bearing posture tasks on the intact side as described in section 2.7.2 (as shown in Fig 2.11). This EMG form the *TA* and *GAS* muscle was used as input to the model-based controller. The model estimated the required torque while performing these tasks and supplied that same torque command to the robotic ankle prosthesis. The ankle angle trajectory of the prosthetic side was compared to the ankle angle trajectory followed by the intact side.

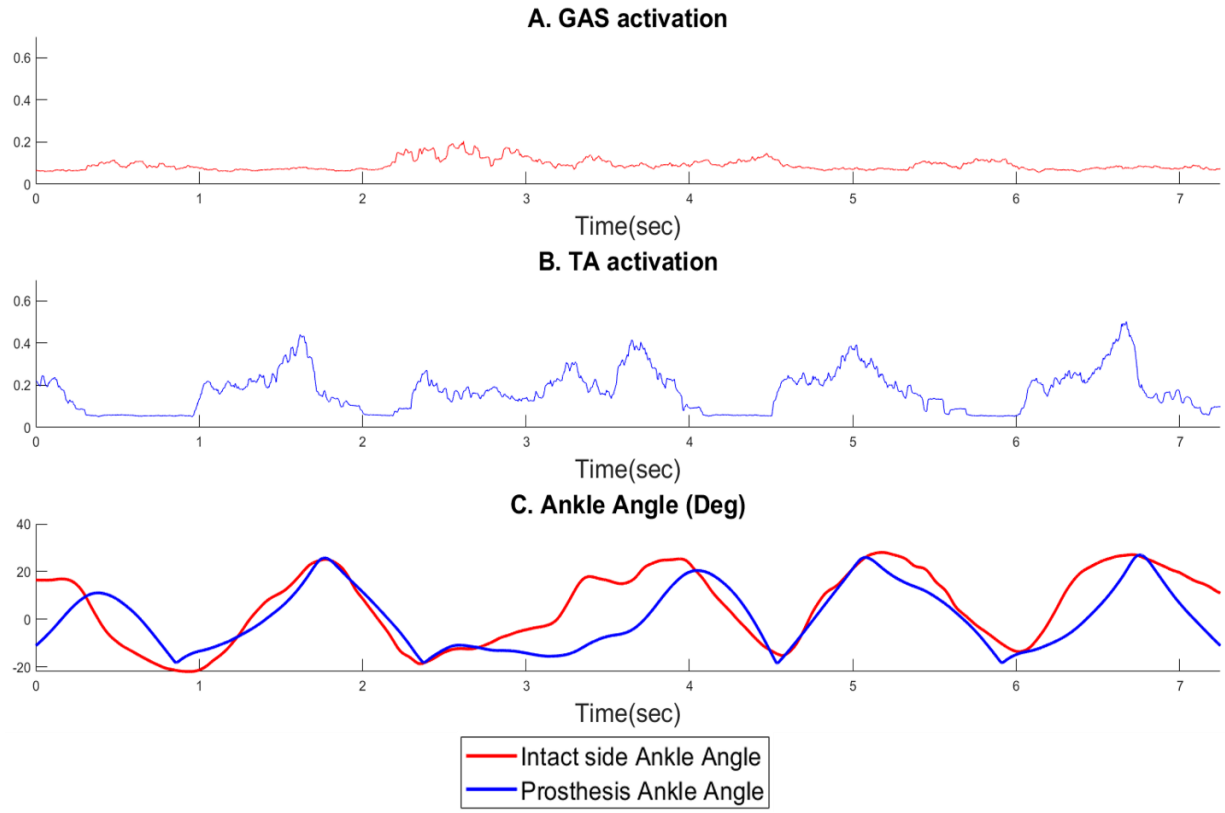

Figure 3.2. Real-time performance of EMG-driven MSK model-based control in open loop performing a simple plantarflexion-dorsiflexion task when the foot was in the air (Fig 2.11 (a)). *A*: Muscle activation of *GAS* on the intact side; *B:* Muscle activation of *TA* on the intact side. They were the inputs of the control. *C*: Prosthesis ankle angle was the output of the control. It was compared to the intact ankle angle (+ve values-dorsiflexion and -ve values-plantarflexion).

Fig 3.2 depicts the performance of the MSK model in real-time when used to perform simple non-weight bearing tasks(Fig 2.11 (a)). From Fig 3.2 C. we can see, that in general the robotic prosthesis ankle angle could follow the intact joint angle. Both motions showed qualitative agreement without the presence of significant delay between the prosthesis side movement and intact side. The ankle angle trajectory of the prosthesis side and intact sides had a R^2 value of 0.62 NRMSE value of 0.202.

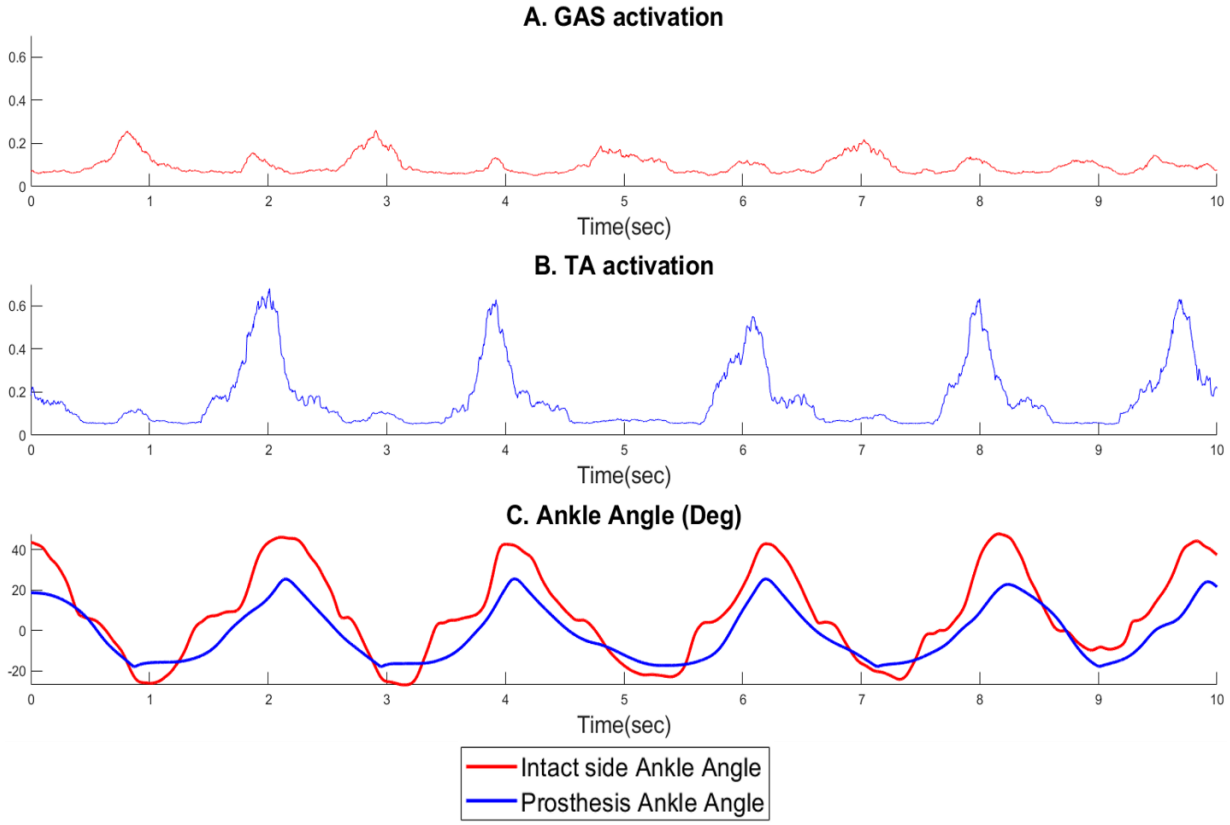

Figure 3.3. Real-time performance of EMG-driven MSK model-based control in open loop performing a simple plantarflexion-dorsiflexion task when the foot was kept on a flat surface (Fig 2.11 (b)). *A*: Muscle activation of *GAS* on the intact side; *B:* Muscle activation of *TA* on the intact side. They were the inputs of the control. *C*: Prosthesis ankle angle was the output of the control. It was compared to the intact ankle angle (+ve values-dorsiflexion and -ve values-plantarflexion).

Fig 3.3 depict the performance of the MSK model in real-time when used to perform simple non-weight bearing tasks(Fig 2.11 (b)). From Fig 3.3 C. we can see, that in general the robotic prosthesis ankle angle could follow the intact joint angle. Both motions showed qualitative agreement with the presence of some delay between the prosthesis side movement and intact side at lower levels of activation. The ankle angle trajectory of the prosthesis side and intact sides had a R^2 value of 0.7749 NRMSE value of 0.1935.

3.4 Real-time closed-Loop Control in weight-bearing symmetric tasks

To evaluate the real-time performance of the control with the device bilaterally symmetric tasks were chosen to test the control. This was done due to the inability of the user to individually activate the tibialis anterior and gastrocnemius muscle when the ankle was fixed in the able-bodied adaptor. To evaluate the capability of this type of continuous control to allow the user to perform unpredictable and non-repetitive tasks, these tasks were chosen - i) Standing on their toes, ii) performing sit-to-stand transitions.

3.4.1 Standing on toes task

Fig 2.12 (a) depicts how the standing on the toes task was performed. Fig 3.4 shows the real-time performance of the control where Fig 3.4 A. and B. shows the TA and GAS muscle activations when the task was performed. Fig 3.4 C. compares the ankle angle trajectory for the intact side and the trajectory followed by the prosthesis side. Table 3.4(a) enlist the normalized root mean square error (NRMSE) and R^2. The angle trajectory showed a high correlation and had a low root mean square error between the intact side and prosthesis side. Fig 3.4 D. compares the biological ankle torque generated on the intact side, the model predicted torque and the prosthesis generated torque. Table 3.4 (b, c) enlist the normalized root mean square error (NRMSE) and R^2 value between the biological ankle torque and model predicted ankle torque and model predicted ankle torque and the prosthesis generated torque.

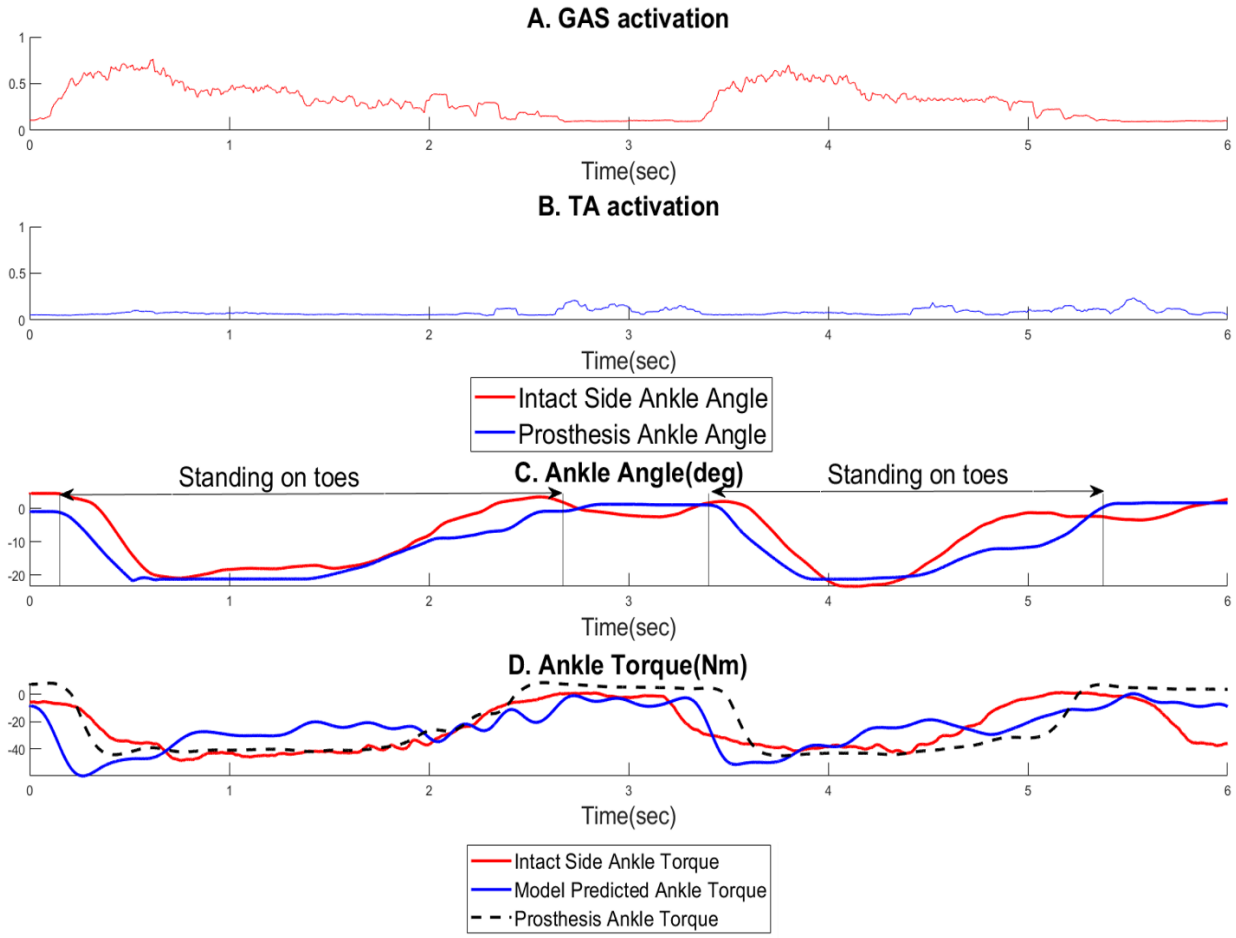

Figure 3.4. Real-time performance for Standing on toes task. A. and B. Muscle activation for *GAS* and *TA* muscles, respectively. C. Comparison of the ankle angle for the intact and prosthetic side (+ve values – dorsiflexion, -ve values – plantarflexion). D. Comparison of ankle torque of the intact side, the model predicted torque and the torque generated by the prosthetic ankle. (+ve values – dorsiflexion torque, -ve values – plantarflexion torque).

Table 3.3 Real-time evaluation of EMG-driven MSK model during standing on toes task.

	Standing on toes task	***NRMSE***	***R^2***
a)	Ankle angle vs Prosthesis angle	0.1461	0.9572
b)	Model predicted torque vs Intact side torque	0.2223	0.8671
c)	Model predicted torque vs Prosthesis torque	0.1044	0.9689

3.4.2 Sit to stand transition task

Fig 2.12 (b) depicts how the standing on the toes task was performed. Fig 3.5 shows the real-time performance of the control where Fig 3.5 A. and B. shows the TA and GAS muscle activations when the task was performed. Fig 3.5 C. compares the ankle angle trajectory for the intact side and the trajectory followed by the prosthesis side. Table 3.5(a) enlist the normalized root mean square error (NRMSE) and R^2. The angle trajectory showed a high correlation and low root mean square error between the intact side and prosthesis side. Fig 3.5 D. compares the

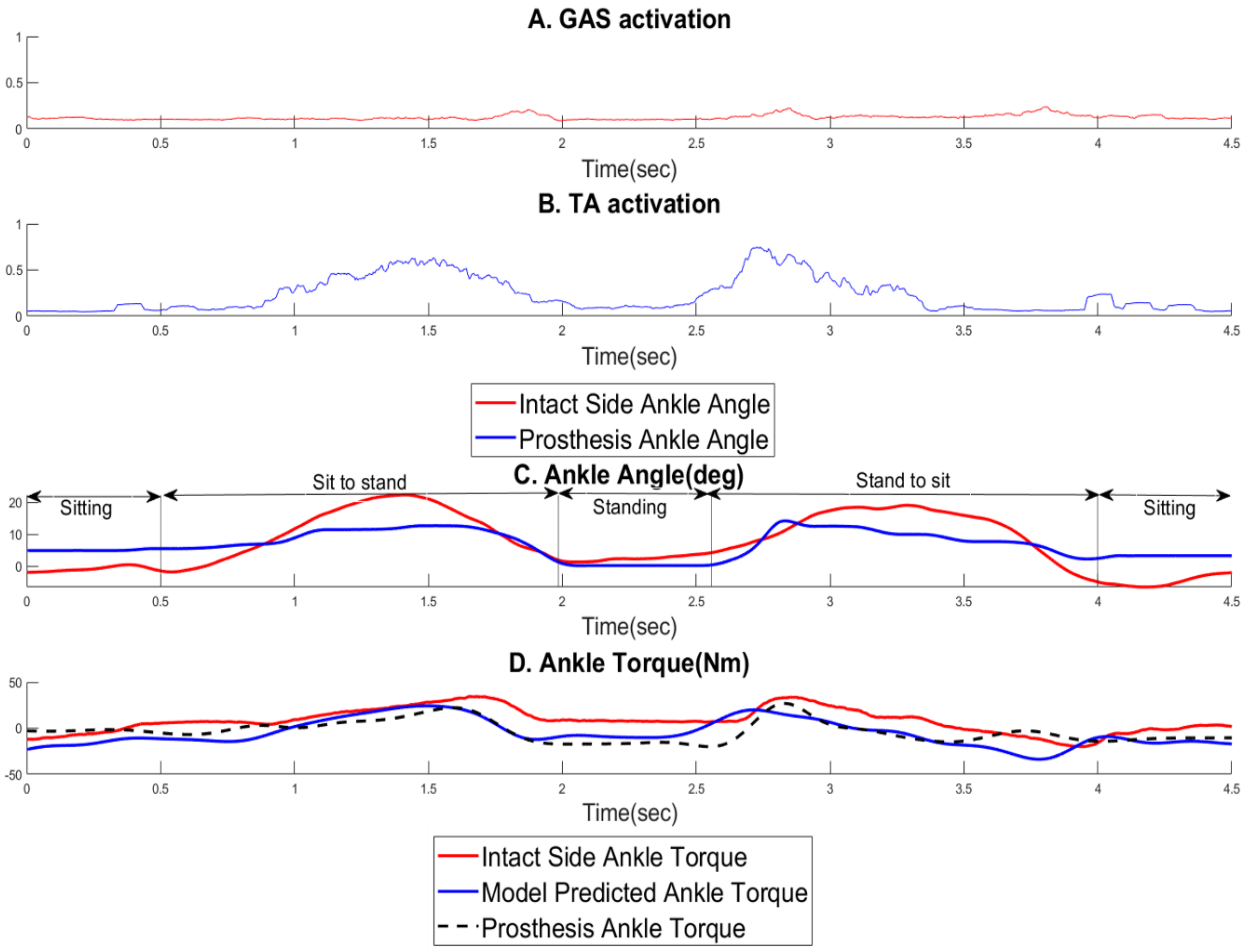

Figure 3.5. Real-time performance for sit-to-stand transitions. A. and B. Muscle activation for *GAS* and *TA* respectively. C. Comparison of the ankle angle for the intact and prosthetic side (+ve values – dorsiflexion, -ve values – plantarflexion). D. Comparison of ankle torque of the intact side, the model predicted torque and the torque generated by the prosthetic ankle. (+ve values – dorsiflexion Torque, -ve values – plantarflexion Torque).

biological ankle torque generated on the intact side, the model predicted torque and the prosthesis generated torque. Table 3.5 (b, c) enlist the normalized root mean square error and R^2 value between the biological ankle torque and model predicted ankle torque and model predicted ankle torque and the prosthesis generated torque. This evaluated the performance of the ankle to replicate the biological kinematics and kinetics of the intact side while performing these non-repetitive, unpredictable tasks.

Table 3.4 Real-time evaluation of EMG-driven MSK model during sit to stand task.

	Sit to stand task	***NRMSE***	***R^2***
a)	Ankle angle vs Prosthesis angle	0.1752	0.6071
b)	Model predicted torque vs Intact side torque	0.41	0.7012
c)	Model predicted torque vs Prosthesis torque	0.1287	0.8921

CHAPTER 4: DISCUSSION AND FUTURESCOPE

4.1 Discussion

The offline simulations enabled us to assess the prediction accuracy of the EMG-driven MSK model across different tasks. For walking at different speeds (1.0m/s and 1.4m/s) and sit-to-stand transitions we observed similar results between our offline analysis and biological ankle torque (Fig 3.1 A., B. & C.). These tasks showed a high correlation between the predictions and biological ankle torque with a high R^2 value and low NRMSE value (Table 3.2). The high prediction accuracy for the walking tasks was expected as the model was trained using walking task data. The prediction accuracy in the case of standing on toes and squatting was relatively low which can be seen from Fig 3.1 D. and E. and the R^2 and NRMSE values listed in Table 3.2. This reduced prediction accuracy in some tasks might be because the model was trained on the data collected during the walking task and it couldn't adapt very well to different tasks that have a different range of motion and torque requirements. Even though the prediction accuracy for other tasks was not great, the advantage of using this type of control – a control where the human is in direct and complete control is that they can modulate their muscle activity to generate the desired prosthesis behavior.

In the second part of the evaluation, when the MSK model was used to control prosthesis in an open loop were the user wore the device and performed non-weight bearing symmetric tasks. Fig 3.2 C. and Fig 3.3 C. shows that the robotic prosthesis ankle angle can follow the intact joint angle when given the *TA* and *GAS* EMG from the intact side as inputs. Both motions showed qualitative agreement without the presence of significant delay between the prosthesis side movement and intact side. Fig 3.3 C. also revealed that the range of motion of the prosthesis device was less than the range of motion of the intact side. This was due to the limitations of the device

used in testing. In this control the model takes EMG and ankle angle as input to estimate the ankle joint torque. Since the dynamics of the human foot are different from the dynamics of the prosthetic ankle, if the same amount of torque was applied in non-weight bearing conditions the output angle may not be similar. But we observed a high correlation with a decent angle tracking performance of the prosthesis ankle angle with the intact side ankle angle. These results imply that this control is capable of allowing the user to freely manipulate the ankle position at will. Even though the prosthesis ankle angle achieved by the device does not match the intact side well, the idea is that since the human is in control, they can modulate the muscle activation to achieve the appropriate angle. This is a particularly useful ability that can allow the users to adjust the ankle angle according to the environment, potentially allowing for better obstacle avoidance, sitting posture, terrain adaptation, etc.

For the final part of the evaluation the two tasks that were chosen were - Standing on toes and sit-to-stand transitions. Fig -3.4 and Fig-3.5 depicts the real-time performance of the control when tasks were performed. Table 3.3 and Table 3.4 compares the NRMSE and R^2 values for averaged torque and angles values for the different conditions tested. Sit-to-stand transitions and standing on toes were tested as they are volitional, non-repetitive tasks, that other autonomous controllers cannot perform or assist with.

As seen in Fig 3.4, in the standing on toes task the prosthesis ankle angle closely follows the intact side ankle angle. Table 3.3(a) also showed a high correlation between the prosthesis angle and intact side ankle angle. The model predicted torque showed a high correlation with the intact side torque and the torque generated by the prosthesis, which can be seen in Table 3.3 (b, c).

As seen in Fig 3.5, in the sit to stand task the prosthesis angle wasn't able to follow the intact side ankle angle very well, even though the prosthesis angle was adjusted to have the

required range of motion. The change in dynamics of the system due to the able-bodied adaptor was believed to be one of the reasons behind this. As seen in Fig 2.10 a. the adaptor allows the able-subject to operate the device with their intact limb, but the intact limb is attached at a slight offset. The way in which the ground reaction force is transferred to the intact limb of the user changes. This leads to the generation of an additional moment about the attachment point making it difficult for the user to load both sides equally while performing the task. The model predicted torque showed a high correlation with the intact side torque and the torque generated by the prosthesis, which can be seen in Table 3.4 (b, c).

Interestingly, in both cases, the accuracy of the MSK model in ankle torque prediction here was higher than the accuracy shown in offline analysis (Table 3.2). Though EMG signals used to generate prosthetic ankle torque were obtained from the intact limb, the improvement in accuracy may be a result of differences between intact and prosthetic limb states (i.e., the joint angles were not identical). The above results showed the feasibility of the real-time control to perform tasks that are non-repetitive and unpredictable. They also showcased the ability to of the system to closely mimic the biological motion and kinetics of the able-bodied joint.

This controller places the human in control of the device which allows us to exploit the intelligence of human beings. Other autonomous controllers cannot react to unknown disturbances. The aso cannot modulate their behavior without the occurrence of change or need to have an inbuilt system to identify the change. Using this voltionalcontroller the user can identify the change in environment and relay the appropriate corrective action to the device by modulating the EMG in their residual muscles and change the dynamics of the device.

4.2 Limitations

Using able-bodied subjects limited the evaluation of the real-time control to bi-laterally symmetric tasks as the user was unable to individually contract their muscles when their foot was fixed in the able-bodied adaptor. Because of this we were unable to test walking like tasks - for which the model was actually trained for.

Using the able-bodied adaptor also changes the dynamics of the system when the user interacts with the device. If an amputee subject were to use the device, then their residual limb would be in-line with the prosthesis and the force would be transferred in that direction. In our case the able-bodied adaptor is not in-line with the device and is at an offset to accommodate the intact foot. This changes the loading conditions and how the force generated by the ankle is transmitted to the able-bodied subject changes. This change in dynamics was not accounted for.

The testing was limited to evaluation of the control with the EMG signal from an intact muscle. For real-world application lower limb amputees need to be able to operate the device with their residual muscles. Also, this type of continuous control requires continuous conscious control of their residual muscle to operate the device. This makes execution of locomotion tasks such as walking difficult and require a lot of training to recruit the appropriate muscle by the appropriate amount at the right time.

4.3 Future Scope

In the future we plan to shift to testing with amputee subjects where their residual muscles will be used to drive the robotic prosthesis. This will allow evaluation of the control using the EMG generated from the residual muscles. Working with amputee subjects would bypass the challenges or limitation of using the able-bodied adaptor and allow asymmetric tasks. Ability to

perform asymmetric tasks would be made possible, as the subjects would control the device using the residual muscles present on the side that the prosthetic foot is attached to.

Aas we have implemented the control on a device that can be configured to be made portable, we would also like to perform tests in the real-world rather than a lab environment. This will help evaluate the controller in more realistic scenarios and also evaluate the full potential of this type of volitional control.

We believe in the future, controllers can be developed that would exploit the advantages of both autonomous and volitional neural controllers, where complex repetive locomotion tasks will be performed by the autonomous controllers and the non-repetitive, unpredictable tasks will be performed by the human through the volitional controller. This will help make these devices real-world applicable.

CHAPTER 5 : CONCLUSION

In this study, we developed an EMG-driven MSK model-based controller for real-time control of a motorized, robotic ankle prosthesis. The model prediction accuracy was evaluated through offline simulations, where the model predicted torque was compared with the biological ankle torque, computed via inverse dynamics. The EMG-driven MSK model was also implemented on a robotic ankle prosthesis and evaluated online. The results showed that the personalized MSK model can accurately predict the ankle joint torque in various task contexts based on the activity of antagonistic ankle muscles. In addition, for the first time, we showed the feasibility of design of robotic ankle control based on biomimicry principles to enable the performance of prosthesis users on tasks that are unpredictable and non-cyclic.

REFERENCES

Archibald, H. (1938). "The heat of shortening and the dynamic constants of muscle." Proceedings of the Royal Society Biological Sciences.

Au, S., M. Berniker and H. Herr (2008). "Powered ankle-foot prosthesis to assist level-ground and stair-descent gaits." Neural Netw **21**(4): 654-666.

Buchanan, T. S., D. G. Lloyd, K. Manal and T. F. Besier (2004). "Neuromusculoskeletal modeling: estimation of muscle forces and joint moments and movements from measurements of neural command." Journal of applied biomechanics **20**(4): 367-395.

Corcos, D. M., G. L. Gottlieb, M. L. Latash, G. L. Almeida and G. C. Agarwal (1992). "Electromechanical delay: An experimental artifact." Journal of Electromyography and Kinesiology **2**(2): 59-68.

Crouch, D. L. and H. Huang (2016). "Lumped-parameter electromyogram-driven musculoskeletal hand model: A potential platform for real-time prosthesis control." J Biomech **49**(16): 3901-3907.

Eilenberg, M. F., H. Geyer and H. Herr (2010). "Control of a powered ankle-foot prosthesis based on a neuromuscular model." IEEE Trans Neural Syst Rehabil Eng **18**(2): 164-173.

Fleming, A. and H. H. Huang (2019). Proportional Myoelectric Control of a Powered Ankle Prosthesis for Postural Control under Expected Perturbation: A Pilot Study. 2019 IEEE 16th International Conference on Rehabilitation Robotics (ICORR).

Fleming, A., S. Huang, E. Buxton, F. Hodges and H. H. Huang (2021). "Direct continuous electromyographic control of a powered prosthetic ankle for improved postural control after guided physical training: A case study." Wearable Technologies **2**: e3.

Fleming, A., N. Stafford, S. Huang, X. Hu, D. P. Ferris and H. H. Huang (2021). "Myoelectric control of robotic lower limb prostheses: a review of electromyography interfaces, control paradigms, challenges and future directions." J Neural Eng **18**(4).

Geyer, H. and H. Herr (2010). "A muscle-reflex model that encodes principles of legged mechanics produces human walking dynamics and muscle activities." IEEE Trans Neural Syst Rehabil Eng **18**(3): 263-273.

Geyer, H. and A. Seyfarth (2016). Neuromuscular Control Models of Human Locomotion. Humanoid Robotics: A Reference. A. Goswami and P. Vadakkepat. Dordrecht, Springer Netherlands**:** 1-30.

Goldfarb, M. (2013). "Consideration of Powered Prosthetic Components as They Relate to Microprocessor Knee Systems." JPO Journal of Prosthetics and Orthotics **25**: P6U P75.

Hagberg, K. and R. Brånemark (2001). "Consequences of non-vascular trans-femoral amputation: a survey of quality of life, prosthetic use and problems." Prosthet Orthot Int **25(**3): 186-194.

Hill, A. (1938). "The heat of shortening and the dynamic constants of muscle." Proceedings of the Royal Society Biological Sciences.

Huang, H., T. A. Kuiken and R. D. Lipschutz (2009). "A strategy for identifying locomotion modes using surface electromyography." IEEE Trans Biomed Eng **56(**1): 65-73.

Huang, H., F. Zhang, L. J. Hargrove, Z. Dou, D. R. Rogers and K. B. Englehart (2011). "Continuous locomotion-mode identification for prosthetic legs based on neuromuscular-mechanical fusion." IEEE Trans Biomed Eng **58**(10): 2867-2875.

Lamoth, C. J., E. Ainsworth, W. Polomski and H. Houdijk (2010). "Variability and stability analysis of walking of transfemoral amputees." Med Eng Phys **32**(9): 1009-1014.

Langlois, K., T. v. d. Hoeven, D. R. Cianca, T. Verstraten, T. Bacek, B. Convens, C. Rodriguez-Guerrero, V. Grosu, D. Lefeber and B. Vanderborght (2018). "EtherCAT Tutorial: An Introduction for Real-Time Hardware Communication on Windows [Tutorial]." IEEE Robotics & Automation Magazine **25**(1): 22-122.

Legro, M. W., G. Reiber, M. del Aguila, M. J. Ajax, D. A. Boone, J. A. Larsen, D. G. Smith and B. Sangeorzan (1999). "Issues of importance reported by persons with lower limb amputations and prostheses." J Rehabil Res Dev **36**(3): 155-163.

Lenzi, T., M. Cempini, L. Hargrove and T. Kuiken (2018). "Design, development, and testing of a lightweight hybrid robotic knee prosthesis." The International Journal of Robotics Research **37**(8): 953-976.

Liu, M., F. Zhang, P. Datseris and H. Huang (2014). "Improving Finite State Impedance Control of Active-Transfemoral Prosthesis Using Dempster-Shafer Based State Transition Rules." Journal of Intelligent & Robotic Systems **76**: 461-474.

Lloyd, D. G. and T. F. Besier (2003). "An EMG-driven musculoskeletal model to estimate muscle forces and knee joint moments in vivo." J Biomech **36**(6): 765-776.

Mengelkoch, L. J., J. T. Kahle and M. J. Highsmith (2017). "Energy costs and performance of transfemoral amputees and non-amputees during walking and running: A pilot study." Prosthet Orthot Int **41**(5): 484-491.

Millard, M., T. Uchida, A. Seth and S. L. Delp (2013). "Flexing computational muscle: modeling and simulation of musculotendon dynamics." J Biomech Eng **135**(2): 021005.

Pan, L., D. L. Crouch and H. Huang (2018). "Myoelectric Control Based on a Generic Musculoskeletal Model: Toward a Multi-User Neural-Machine Interface." IEEE Transactions on Neural Systems and Rehabilitation Engineering **26**(7): 1435-1442.

Schmalz, T., S. Blumentritt and R. Jarasch (2002). "Energy expenditure and biomechanical characteristics of lower limb amputee gait: the influence of prosthetic alignment and different prosthetic components." Gait & posture **16**(3): 255-263.

Sup, F., H. A. Varol, J. Mitchell, T. J. Withrow and M. Goldfarb (2009). "Self-Contained Powered Knee and Ankle Prosthesis: Initial Evaluation on a Transfemoral Amputee." IEEE ... International Conference on Rehabilitation Robotics : [proceedings] **2009**: 638-644.

Tahir, U., A. L. Hessel, E. R. Lockwood, J. T. Tester, Z. Han, D. J. Rivera, K. L. Covey, T. G. Huck, N. A. Rice and K. C. Nishikawa (2018). "Case Study: A Bio-Inspired Control Algorithm for a Robotic Foot-Ankle Prosthesis Provides Adaptive Control of Level Walking and Stair Ascent." Frontiers in Robotics and AI **5**(36).

Upadhye, S., C. Shah, M. Liu, G. Buckner and H. H. Huang (2021). A Powered Prosthetic Ankle Designed for Task Variability - A Concept Validation. International Conference on Intelligent Robots and Systems. Prague.

Varol, H. A., F. Sup and M. Goldfarb (2010). "Multiclass real-time intent recognition of a powered lower limb prosthesis." IEEE transactions on bio-medical engineering **57**(3): 542-551.

Vivian, H. A. (1938). "The heat of shortening and the dynamic constants of muscle." Proceedings of the Royal Society B Biological Sciences.

Winters, J. M. (1990). Hill-Based Muscle Models: A Systems Engineering Perspective. Multiple Muscle Systems: Biomechanics and Movement Organization. J. M. Winters and S. L. Y. Woo. New York, NY, Springer New York**:** 69-93.

Zajac, F. E. (1989). "Muscle and tendon: properties, models, scaling, and application to biomechanics and motor control." Crit Rev Biomed Eng **17**(4): 359-411.

APPENDICES

Appendix A

Nomenclature

$\boldsymbol{e(t)}$	:	*Raw EMG signal*
$\boldsymbol{\alpha}$	:	*Neural activation second order dynamics constant*
$\boldsymbol{\beta_1}$	:	*Neural activation second order dynamics constant*
$\boldsymbol{\beta_2}$	:	*Neural activation second order dynamics constant*
$\boldsymbol{u(t)}$	:	*Neural activation*
$\boldsymbol{a(t)}$	:	*Muscle activation*
$\boldsymbol{A}$	:	*Non-linear shape factor*
$\boldsymbol{d}$	:	*Electromechanical delay*
$\boldsymbol{r_{max}}$	:	*Max muscle moment arm*
$\boldsymbol{r}$	:	*Muscle moment arm*
$\boldsymbol{\theta}$	:	*Ankle Angle*
$\boldsymbol{\theta_{max}}$	:	*Ankle angle when moment arm is maximum in length*
$\boldsymbol{\theta_{ref}}$	:	*Ankle angle when muscle fiber length is equal optimal fiber length*
$\boldsymbol{\phi}$	:	*Pennation angle*
$\boldsymbol{\phi_{ref}}$	:	*Pennation angle when muscle fiber length is equal to optimal fiber length*
$\boldsymbol{l_{slack}}$	:	*Tendon slack length*
$\boldsymbol{l_o}$	:	*Optimal muscle fiber length i.e., muscle fiber length when muscle generates peak force*
$\boldsymbol{l_{mt}}$	:	*Muscle unit length*
$\boldsymbol{l_{ce}}$	:	*Length of contractile element*
$\boldsymbol{l_{se}}$	:	*Length of series elastic element*
$\boldsymbol{v_{mt}}$	:	*Velocity of muscle unit*
$\boldsymbol{v_{ce}}$	:	*Velocity of contractile element*
$\boldsymbol{F_{ce}}$	:	*Force generated by contractile element*
$\boldsymbol{F_l(l_{ce})}$	:	*Force-length relationship*
$\boldsymbol{w}$	:	*Curve width parameter*
$\boldsymbol{F_v(v_{ce})}$	:	*Force-velocity relationship*

$\boldsymbol{F_{max}}$	:	*Peak isometric force*
$\boldsymbol{v_{max}}$	:	*Max velocity of contraction*
$\boldsymbol{N}$	:	*Dimensionless force factor*
K	:	*Shape factor*
$\boldsymbol{F_{pe}}$	:	*Force generated by parallel elastic element*
$\boldsymbol{\epsilon_{pe}}$	:	*Parallel elastic element strain*
$\boldsymbol{F_{m}}$	:	*Force generated by muscle unit*
$\boldsymbol{\tau_{m}}$	:	*Torque generated by muscle unit*
$\boldsymbol{F_{m(dorsi)}}$	:	*Force generated by the dorsiflexor muscle unit*
$\boldsymbol{r_{dorsi}}$	:	*Dorsiflexor moment arm*
$\boldsymbol{F_{m(plant)}}$	:	*Force generated by the plantarflexor muscle unit*
$\boldsymbol{r_{plant}}$	:	*Plantarflexor moment arm*
$\boldsymbol{\tau_{ankle}}$	:	*Model predicted ankle torque*
$\boldsymbol{\tau_{bio}}$	:	*Biological ankle torque*